

Clump-Scale Dust Attenuation in Epoch of Reionization Galaxies: Spatially Resolved Properties from FirstLight Simulations

YURINA NAKAZATO,^{1,2} KOSEI MATSUMOTO,³ AKIO K. INOUE,^{4,5} DANIEL CEVERINO,^{6,7} TAKASHI HOSOKAWA,⁸ AND DAISUKE TOYOUCHI⁹

¹Center for Computational Astrophysics, Flatiron Institute, 162 5th Avenue, New York, NY 10010

²Department of Physics, The University of Tokyo, 7-3-1 Hongo, Bunkyo, Tokyo 113-0033, Japan

³Sterrenkundig Observatorium Department of Physics and Astronomy Universiteit Gent, Krijgslaan 281 S9, B-9000 Gent, Belgium

⁴Waseda Research Institute for Science and Engineering, Faculty of Science and Engineering, Waseda University, 3-4-1 Okubo, Shinjuku, Tokyo 169-8555, Japan

⁵Department of Physics, School of Advanced Science and Engineering, Faculty of Science and Engineering, Waseda University, 3-4-1, Okubo, Shinjuku, Tokyo 169-8555, Japan

⁶Departamento de Fisica Teorica and CIAFF, Facultad de Ciencias, Universidad Autonoma de Madrid, Cantoblanco, 28099 Madrid, Spain

⁷CIAFF, Facultad de Ciencias, Universidad Autonoma de Madrid, 28049 Madrid, Spain

⁸Department of Physics, Graduate School of Science, Kyoto University, Sakyo, Kyoto 606-8502, Japan

⁹Theoretical Astrophysics, Department of Earth and Space Science, The University of Osaka, 1-1 Machikaneyama, Toyonaka, Osaka 560-0043, Japan

ABSTRACT

Understanding dust attenuation in galaxies at both integrated and spatially resolved scales is fundamental for accurately determining the physical properties of galaxies. Recent high-spatial-resolution observations with ALMA and JWST enable investigations of spatially resolved properties in high-redshift galaxies ($z \gtrsim 6$), but spatial variations in dust properties remain poorly constrained. We use cosmological zoom-in simulations combined with post-processing dust radiative transfer calculations for 376 clumpy galaxies at $z = 6$ -9 with stellar masses of $M_* \gtrsim 10^9 M_\odot$. For each system, we investigate dust attenuation and re-emission properties for three components: system-integrated, individual clumps, and diffuse regions. We find that system-integrated attenuation curves are grayer than the Calzetti curve, even when assuming MW- or SMC-type dust. Attenuation curves of individual clumps are even grayer, while diffuse regions exhibit steeper curves owing to enhanced scattering in optically thin environments. Since the effects of optical depth and dust-star geometry are intrinsically degenerate in attenuation curves, we introduce a toy model based on the IRX- $\Delta\beta$ plane, where $\Delta\beta$ denotes the difference between attenuated and intrinsic UV slopes. Applying this framework, we find that clumps have dust column densities approximately an order of magnitude higher than system-integrated values and exhibit co-spatial or dust-extended geometries. In contrast, system-integrated attenuation reflects star-extended geometries driven by contributions from optically thin diffuse regions. We apply this framework to REBELS-IFU galaxies at $z \sim 7$ and find good agreement with our simulation predictions.

1. INTRODUCTION

Astrophysical dust is a key component of the interstellar medium (ISM) in galaxies. The composition and size distribution of dust grains determine the wavelength dependence of absorption and scattering, which, combined with the spatial distribution of dust relative to radiation sources (e.g., stars), determines the overall attenuation. The attenuated emissions are re-radiated as infrared (IR) radiation. This dust attenuation and re-emission shapes the observed spectral energy distributions (SEDs) of galaxies.

Understanding dust attenuation and re-emission is crucial for accurately measuring fundamental galaxy properties. The shape of the dust attenuation curve, typically characterized

by the ratio of attenuation at different wavelengths (e.g., A_{UV}/A_V), is essential for correcting observed fluxes and deriving intrinsic properties such as stellar masses and star formation rates (SFRs). The UV continuum slope (β_{UV}), defined through $f_\lambda \propto \lambda^{\beta_{\text{UV}}}$ (Calzetti et al. 1994), is widely used as an indicator of dust attenuation. Absorbed UV and optical photons are re-emitted in the IR, and the ratio of total IR to UV luminosity ($\text{IRX} \equiv L_{\text{IR}}/L_{\text{UV}}$) provides a measure of dust obscuration, often evaluated through the IRX- β_{UV} relation (Meurer et al. 1999).

The advent of JWST and ALMA has revolutionized our ability to study dust properties during the epoch of reionization (EoR, $z \simeq 6$ -9). JWST spectroscopic observations provide rest-frame UV-to-optical continua, enabling direct measurements of attenuation curves for individual galaxies (e.g., Markov et al. 2025; Shvaei et al. 2025; Markov et al. 2023; Fisher et al. 2025). These observations reveal that attenuation curves at the EoR are systematically flatter than the

empirical Calzetti curve, while UV bump detections provide constraints on dust composition (e.g., Witstok et al. 2023). Complementary ALMA observations in the far-IR measure dust temperatures and total IR luminosities (e.g., Sommovigo et al. 2022; Mitsuhashi et al. 2024; Algera et al. 2024; Inoue et al. 2020; Inami et al. 2022), showing increasing dust temperatures at higher redshifts and deviations from the canonical IRX– β_{UV} relations.

Beyond galaxy-integrated measurements, spatially resolved observations are beginning to reveal significant variations in dust properties within individual high-redshift galaxies. High-resolution JWST/NIRCam photometry enables pixel-by-pixel SED fitting to generate maps of A_V and β_{UV} (e.g., Abdurro'uf et al. 2023; Giménez-Arteaga et al. 2023, 2024; Sun et al. 2024; Tanaka et al. 2024; Lines et al. 2025), while NIRSpec IFU observations allow construction of Balmer decrement maps through $\text{H}\alpha/\text{H}\beta$ ratios (e.g., Parlanti et al. 2025; Ishikawa et al. 2025; Mawatari et al. 2025). These observations commonly reveal clumpy morphologies in EoR galaxies (e.g., Chen et al. 2023; Hainline et al. 2024; Shibuya et al. 2024; Lines et al. 2025; Harikane et al. 2025), and ongoing programs (e.g., RIOJA:GO-1840, GA-NIFS:GTO, REBELS-IFU:GO-1626) are beginning to resolve physical properties of individual clumps and diffuse components. These advances in resolving sub-galactic structure enable us to address fundamental questions about the spatial variations of dust properties and the physical processes that drive them.

On the theoretical side, cosmological simulations combined with dust radiative transfer (RT) have made significant progress in reproducing observed dust properties of high-redshift galaxies. Previous studies have investigated system-integrated properties such as attenuation curves (Narayanan et al. 2018a), dust temperatures (Liang et al. 2019; Vijayan et al. 2019), and IRX– β_{UV} relations (Narayanan et al. 2018b; Liang et al. 2021a; Vijayan et al. 2019; Pallottini et al. 2022; Behrens et al. 2018; Mushtaq et al. 2023). However, these studies have focused exclusively on galaxy-integrated measurements and have not explored how dust properties vary spatially within galaxies, specifically how individual star-forming regions (clumps) differ from diffuse components and system-integrated values. This gap becomes critical as spatially resolved observations become increasingly common. If dust properties differ significantly between clumps and their host galaxies' integrated values, analyses that assume uniform properties across a galaxy may yield systematically biased estimates of stellar masses, ages, and star formation rates.

In this paper, we investigate how dust attenuation (β_{UV} , A_V , attenuation curves) and reemission properties (IRX, T_d) vary spatially within high-redshift clumpy galaxies using cosmological zoom-in simulations. We analyze massive galaxies ($M_* \sim 10^{8-10} M_\odot$) at $z = 6-9$, combined with post-processing dust radiative transfer calculations using SKIRT (Baes et al. 2011). We identify 376 clumpy systems containing 1059 individual star-forming clumps ($R \gtrsim 100 \text{ pc}$, $\text{SFR} \gtrsim 1 M_\odot \text{ yr}^{-1}$) based on SFR surface density.

For each system, we analyze dust properties separately for clumps, diffuse regions, and system-integrated values. To disentangle the effects of optical depth and dust-star geometry on the observed variations, we develop a toy model that utilizes the IRX– $\Delta\beta$ plane ($\Delta\beta \equiv \beta_{\text{UV}} - \beta_{\text{UV},0}$, the difference between attenuated and intrinsic UV slopes) with two key parameters: dust optical depth (i.e., dust column density) and the dust-to-star scale-height ratio.

This paper is organized as follows. Section 2 describes our simulation setup, dust radiative transfer calculations, and clump identification method. Section 3 presents spatially resolved dust properties for an example galaxy and statistical results for all clumpy systems. Section 4 develops the toy model to interpret observed variations and discusses implications for observations. We summarize our findings in Section 5.

2. METHOD

2.1. Cosmological Zoom-in Simulations: *FirstLight*

We use the cosmological zoom-in simulation suite *FirstLight*. The simulations used in this work were first presented in Ceverino et al. (2017) and have already been used to study several high-redshift topics, including galaxy morphologies (Ceverino et al. 2021; Nakazato et al. 2024; Dome et al. 2024), star formation histories (Ceverino et al. 2018, 2024), chemical evolution (Langan et al. 2020; Nakazato et al. 2023), UV/IR continuum emission (Ceverino et al. 2019; Mushtaq et al. 2023), and size evolution (Cataldi et al. 2025, Ceverino in prep.).

We use the simulation code ART, which employs Adaptive Mesh Refinement (AMR; Kravtsov et al. 1997; Kravtsov 2003; Ceverino & Klypin 2009a), with a parent cosmological box of side length 40 comoving Mpc/h. Initial conditions were generated with MUSIC (Hahn & Abel 2011) at $z = 150$ using a Planck cosmology (Planck Collaboration et al. 2014). We select all dark matter halos with a maximum circular velocity greater than $V_{\text{circ}} = 178 \text{ km s}^{-1}$ at $z = 5$, resulting in a sample of 62 halos. For each halo, we perform zoom-in simulations with a dark matter particle mass of $8 \times 10^4 M_\odot$ and a minimum stellar particle mass of $10^3 M_\odot$. All simulations were evolved down to $z = 5.25$. The smallest cell size achieved is $\Delta x_{\text{min}} = 31 \text{ pc}$ ($7/(1+z)$). To prevent artificial fragmentation at the smallest cell scale, a pressure floor is imposed to ensure that the Jeans length is always resolved by at least seven cells (Ceverino et al. 2010, also see Appendix B of Nakazato et al. 2024).

Stars form in high-density ($\rho > \rho_{\text{th}}$) and low-temperature ($T < T_{\text{th}}$) gas cells. In our simulations, we adopt thresholds of $\rho_{\text{th}} = 0.035 M_\odot \text{ pc}^{-3}$ ($n_{\text{th}} = 1 \text{ cm}^{-3}$) and $T_{\text{th}} = 10^4 \text{ K}$. We adopt a stochastic model in which the probability scales with the gas free-fall time (Ceverino & Klypin 2009b). This prescription ensures that higher-density gas cells are more likely to form stars, resulting in the Kennicutt–Schmidt relation (Kennicutt 1998). Our simulations follow radiative cooling by atomic hydrogen and helium, metal ions and atoms, and molecular hydrogen calculated using CLOUDY (Ferland et al. 1998). We also include photoionization heating by the

redshift-dependent UVB with partial self-shielding (Haardt & Madau 1996).

In the FirstLight simulations, we incorporate the following stellar feedback mechanisms: supernovae (SNe) and stellar winds, radiation pressure on dust grains that absorb UV photons, and infrared (IR) radiation pressure via a subgrid model. The first two are implemented as thermal pressure terms with a constant heating rate for 40 Myr, whereas the latter two are implemented as non-thermal pressure terms (Ceverino et al. 2014). In addition to thermal feedback, we include the injection of momentum from the (unresolved) expansion of gaseous shells driven by SNe and stellar winds (Ostriker & Shetty 2011). Further details can be found in Ceverino et al. (2017).

The 62 galaxies in our sample have stellar masses greater than $\sim 10^{10} M_{\odot}$ at $z = 5$. The maximum resolution in the zoom-in hydrodynamical simulations, particularly in dense clumps, enables us to resolve gas densities of $\sim 10^3 \text{ cm}^{-3}$ with temperatures of $\sim 300 \text{ K}$. We stored a total of 66 snapshots from $z = 9.5$ to $z = 5.25$ for each galaxy, with spacing in the cosmic expansion parameter of $\Delta a = 0.001$, corresponding to 7-10 Myr. This frequent output cadence is sufficient to follow dynamics during galaxy mergers and subsequent clumpy phase that occur within a dynamical timescale (Nakazato et al. 2024).

2.2. Post-Processing Radiative Transfer

Dust attenuation of the all simulated galaxies (62 galaxies, 4092 snapshots) is calculated by using the post-processing radiative transfer code SKIRT (Baes et al. 2011; Camps & Baes 2020). SKIRT is an open-source, three-dimensional Monte Carlo dust RT code that self-consistently calculates dust temperatures and re-emission by accounting for both absorption and anisotropic scattering processes. To perform the RT calculations, we specify the stellar emission properties (Section 2.2.1), dust spatial distribution (Section 2.2.2), and adopted dust composition and grain-size distributions (Section 2.2.3) as input parameters.

2.2.1. Stellar Emission

We construct the SEDs of individual stellar particles using single stellar population (SSP) models from BPASS (Eldrige et al. 2017), based on the mass, age, and metallicity of each stellar particle. Each stellar particle is treated as a single starburst. Among the BPASS models, we adopt a Chabrier IMF with an upper mass limit of $300 M_{\odot}$.

For stellar particles younger than 15 Myr, we reassign their ages following Nakazato et al. (2023). This adjustment is needed because our simulations form stellar particles with a fixed time step of $\Delta t_{\text{SF}} = 5 \text{ Myr}^1$, while the simulation output times are not synchronized with this interval. The reassignment accounts for continuous star formation within each discrete timestep.

¹ The time step width in the simulation is much shorter than this, typically 1000 yr.

We note that we do not consider nebular continuum emission. Recent JWST observations suggest that nebular emission may dominate the UV continuum in some systems (e.g., Cameron et al. 2024), and several theoretical studies have investigated the effect of nebular continuum (e.g., Inoue 2011; Ceverino et al. 2019; Katz et al. 2025; Narayanan et al. 2025a; Newman et al. 2026). In particular, Yanagisawa et al. (2025) and Katz et al. (2025) demonstrate that HII regions around very young stars (ages $\sim 1\text{--}5$ Myr) have dominant nebular continuum emission that makes UV slopes redder ($\beta_{\text{UV}} \sim -2.5$), while stellar continuum alone produces bluer slopes ($\beta_{\text{UV}} \sim -2.5$ to -3). However, the contribution of nebular continuum becomes negligible for stellar ages older than ~ 10 Myr. Since most of the clumps we identified have ages $\gtrsim 30$ Myr (top panel of Figure 1), we expect that nebular continuum does not significantly affect the UV slopes or the IR re-emission calculated in our analysis. We will investigate the contribution of nebular continuum for all FirstLight simulations in future work.

The SED (including both stellar and dust emission) is sampled using 150 logarithmically spaced wavelength bins, covering the range from 0.1 to $1000 \mu\text{m}$. To ensure good convergence, a total of 10^7 photon packets per wavelength bin are emitted from the stars in each calculation. The numerical convergence with respect to the number of photon packets and the wavelength binning is verified in Appendix A.

2.2.2. Dust Spatial Distribution

The spatial distribution of dust is imported from the hydrodynamical simulation by assuming that the dust distribution scales with that of metals, according to the fraction $\text{DTM} = M_{\text{dust}}/M_{\text{metal}}$. We adopt a fixed value of $\text{DTM} = 0.4$, which is used in several high- z simulation studies (e.g., Behrens et al. 2018; Lovell et al. 2021; Mushtaq et al. 2023). This value is also consistent with the analytical estimates by Dayal et al. (2022), who derived $\text{DTM} \sim 0.32\text{--}0.4$ for observed $z \sim 7$ galaxies with dust continuum detections by ALMA (i.e., REBELS galaxies). Since the galaxies in our simulated sample have stellar masses of $M_{\star} \gtrsim 10^9 M_{\odot}$ at $z \sim 7$, comparable to the ALMA-observed systems, the adopted DTM value is reasonable.

2.2.3. Dust Absorption, Scattering and Re-emission

The size distribution and composition of the dust affect its absorption and scattering properties (e.g., Draine et al. 2014). We adopt dust models of Weingartner & Draine (2001) that are appropriate for the extinction curve of Milky Way (MW) and Small Magellanic Cloud (SMC). The grain size distribution of graphite/silicate/PAH for MW and SMC is sampled using 10/10/10 and 10/10/0 bins, respectively. The exact nature of the dust grains in high-redshift galaxies is a matter of ongoing debate. Recent JWST observations investigate dust attenuation curves at $z > 4$ galaxies (Fisher et al. 2025; Ormerod et al. 2025; Witstok et al. 2023; Markov et al. 2023, 2025) and find that 20-25% of REBELS and JADES samples exhibit evidence for a 2175Å bump, which might be originated from carbonaceous grain including Polycyclic Aro-

matic Hydrocarbons (PAHs, see Li et al. 2024; Lin et al. 2025; Nanni et al. 2025) as seen in MW extinction curves (Cardelli et al. 1989), but not seen in SMC’s one (Gordon et al. 2003). We, therefore, choose these two models and set MW-dust type as a default model. The corresponding results for SMC-dust are shown in Appendix C.

We consider the self-absorption of dust emission, which becomes important in dense clouds with large optical depths. In Appendix A, we compare the results with and without self-absorption effects. We also include the transient heating function to calculate non-local thermal equilibrium (NLTE) dust emission from stochastically heated small grains and PAH molecules (Camps & Baes 2015). SKIRT outputs the mass-weighted dust temperature for each cell;

$$T_{\text{cell}} = \frac{\sum_i \rho_{\text{cell},i} T_{\text{cell},i}}{\sum_i \rho_{\text{cell},i}}, \quad (1)$$

where $\rho_{\text{cell},i}$ is the mass density of dust type i , and $T_{\text{cell},i}$ is the dust temperature for type i dust in a cell that are obtained through the energy balance equation. We also include dust heating from CMB radiation, which at high-redshifts CMB temperature increases as $T_{\text{CMB}}(z) = (1+z) \times T_{\text{CMB}(z=0)}$, and becomes non-negligible (da Cunha et al. 2015).

The radiative transfer calculations are iterated until the IR re-emission luminosity converges within 3%, or until a maximum of seven iterations is reached. An octree structure is used to construct the spatial grids of dust media, where cells are recursively subdivided until each contains less than 10^{-6} of the total dust mass. The highest grid level corresponds to a cell width of ~ 4.9 pc, approximately one-fourth of the minimal cell size in the hydrodynamical simulation.

2.3. Clump Identification

In order to quantitatively evaluate how dust properties vary spatially, we categorize each galaxy into three components: (1) the *system-integrated* component, representing the entire galaxy within a projected $10 \text{ kpc} \times 10 \text{ kpc}$ region; (2) individual *star-forming clumps*, identified based on SFR surface density thresholds; and (3) the *diffuse* component, defined as the system-integrated region with identified clumps masked out, which includes tidal tails, bridges, and inter-clump regions. This categorization allows us to investigate whether and how local physical conditions (dust-star geometry, dust column density) affect dust attenuation and re-emission properties such as temperature, UV slope, and attenuation curve shape.

We identify star-forming clumps based on the surface density of the star formation rate, following Nakazato et al. (2024). Here, we briefly summarize the procedure. Clumps are identified in two-dimensional “images” constructed by projecting a cubic region with a fixed side length of 10 kpc along the line of sight. The gas and stellar masses are reassigned to a uniform grid with a cell size of $\Delta = 50$ pc.

To identify ~ 100 pc-scale star-forming clumps comparable to those observed with JWST, we adopt a threshold SFR surface density of $\Sigma_{\text{SFR}} = 10^{1.5} M_{\odot} \text{ yr}^{-1} \text{ kpc}^{-2}$ per grid.

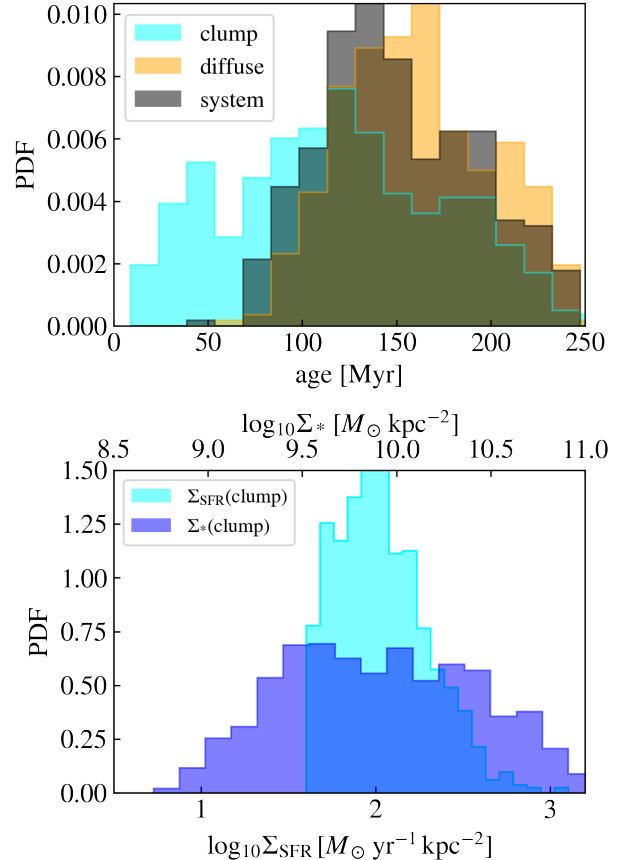


Figure 1. Histogram of clump properties. The top panel shows the mass-weighted stellar age distributions for each component: clumps (cyan), diffuse (orange), and system-integrated (black). The bottom panel shows the surface density distributions of SFR (cyan) and stellar mass (blue) for clump components. Note that these surface densities are only well-defined for clumps due to their compact nature.

Clumps are identified above this threshold using a dendrogram technique (Rosolowsky et al. 2008). Groups with at least $N_{\text{grid}} = 16$ grid cells are identified as clumps, allowing us to detect clumps with radii of $\gtrsim 100$ pc and $\text{SFR} \gtrsim 1 M_{\odot} \text{ yr}^{-1}$, corresponding to observed clumps with the intrinsic [OIII] 5007 fluxes of $\sim 3 \times 10^{-18} \text{ erg s}^{-1} \text{ cm}^{-2}$.

Among 4092 snapshots at $z = 9.5-5.5$, we identify 376 snapshots in the clumpy phase, defined as systems containing at least two clumps. In total, 1059 clumps are identified in these systems. Figure 1 shows the physical properties of clumps from these clumpy systems. The top panel shows the mass-weighted stellar age distributions for each component: clumps (cyan), diffuse regions (orange), and system-integrated (black), with mean values of 118 Myr, 158 Myr, and 145 Myr, respectively. The clump age distribution is bimodal, with peaks at $\lesssim 50$ Myr and $\gtrsim 50$ Myr; the younger population primarily forms in tidal tails during mergers, as explained in Nakazato et al. (2024). The bottom panel shows the stellar mass surface density (blue, upper x-axis) and SFR

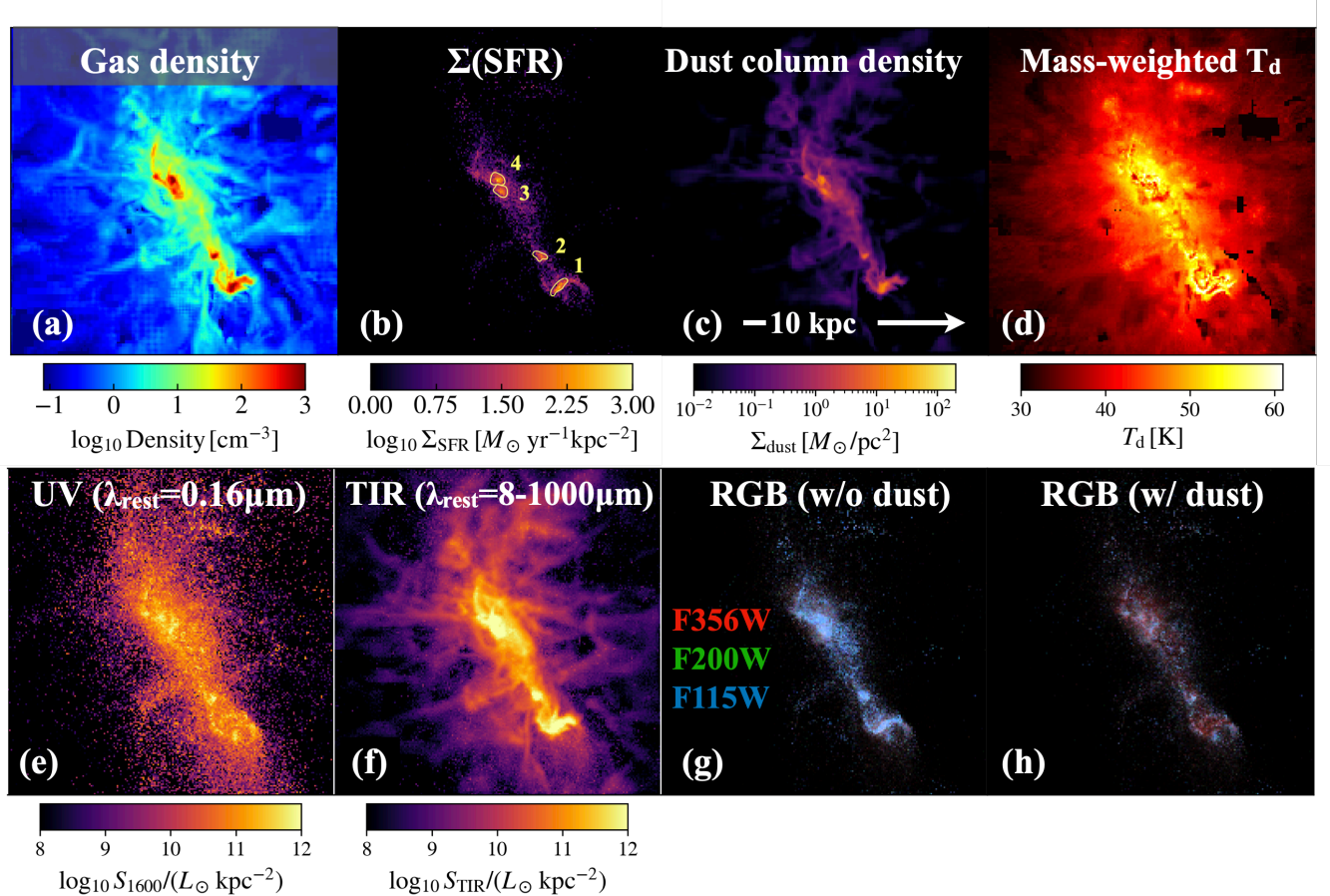


Figure 2. Projected distribution of simulated galaxy FL957 at $z = 7.7$, one of the identified clumpy galaxies. *Upper panels:* (a) projected gas number density, (b) surface SFR density with yellow lines identifying star-forming clumps (see Section 2.3), (c) dust column density, and (d) mass-weighted dust temperature. *Lower panels:* (e) rest-frame UV surface brightness (νL_ν at 1600 Å), (f) total IR emission integrated over $\lambda_{\text{rest}} = 8\text{--}1000\mu\text{m}$, (g) mock JWST/NIRCam three-color image (F115W, F200W, F356W) without dust attenuation, and (h) the same with dust attenuation. Each panel shows a $10\text{ kpc} \times 10\text{ kpc}$ region with a projected depth of 10 kpc.

surface density (cyan, lower x-axis) distributions for clumps. The median values are $\log_{10} \Sigma_* [M_\odot \text{ kpc}^{-2}] = 9.9$ and $\log_{10} \Sigma_{\text{SFR}} [M_\odot \text{ yr}^{-1} \text{ kpc}^{-2}] = 2.0$, respectively, indicating compact star-forming clumps. These 376 clumpy systems are used for the statistical analysis in the following sections.

3. RESULT

3.1. Dust Properties of an Individual Clumpy Galaxy: FL957 at $z = 7.7$

In this section, we present one representative example: FL957 at $z = 7.7$, which was also introduced in Nakazato et al. (2024) and has four clumps within a 10×10 kpc region. The physical properties of each clump, such as stellar mass, mass-weighted age, and clump radius, are tabulated in Table B.1. The clumpy systems were formed during the merger phase.

Figure 2 shows the projected maps of physical properties of FL957. Among the four clumps, two clumps formed within a tidal tail produced by the peri-center passage of two galaxies. Each clump has high gas densities of $\simeq 200$

400 cm^{-3} as shown in panel (a), triggering intense star formation with surface densities $\simeq 60\text{--}115 M_\odot \text{ yr}^{-1} \text{ kpc}^{-2}$ (panel (b)). Such clumps are bright in [OIII] 5007Å (see Figure 2 of Nakazato et al. (2024)). A fraction of these newly formed stars end their lives as Type II SNe, enriching the surrounding gas with metals and producing large amounts of dust. The distribution of dust column density in panel (c) therefore traces the distributions of gas density and surface SFR density, reflecting the enhanced dust production in regions of bursty star formation. The mass-weighted dust temperature in panel (d) shows elevated temperatures ($T_{\text{d, mass}} \sim 50\text{--}60 \text{ K}$) in the clumps, where intense star formation heats the dust locally. The surrounding diffuse regions exhibit lower temperatures ($T_{\text{d, mass}} \sim 40\text{--}45 \text{ K}$), reflecting the lower radiation field intensities away from the star-forming sites. The dust in these regions absorbs UV/optical photons and re-emits them as IR radiation, and the IR map in panel (f) also corresponds to this distribution. The UV emission in panel (e) is a noisier image in comparison to the IR image, due to the scattering effect of

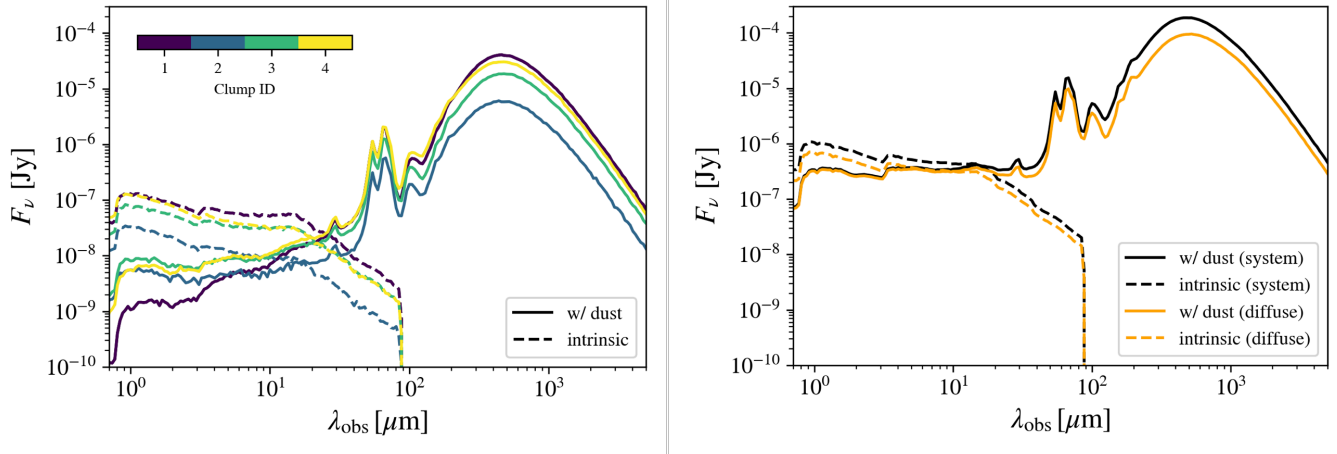


Figure 3. *Left:* SEDs for the four clumps. The dashed and solid lines indicate the intrinsic stellar continuum and the attenuated (with re-emission) SEDs, respectively. *Right:* SEDs for the system-integrated (black) and diffuse (orange) components. The system-integrated SED is calculated over the entire $10 \text{ kpc} \times 10 \text{ kpc}$ region, while the diffuse component SED is obtained by subtracting the clump emission from the system-integrated value.

UV photons. In the NIRCam RGB images (panels (g) and (h)), although the intrinsic UV clumps are colocated with the *physical* star-forming clumps, the dust-attenuated images show smaller clumps. This is because the clumps have high dust column densities ($A_V = 1.1\text{--}2.8$) that heavily attenuate UV radiation, whereas the surrounding diffuse gas has much lower attenuation ($A_V \sim 0.09$). Such effects are seen in several simulated galaxies (Ceverino et al. in prep.), but also in observations (e.g., Bowler et al. 2022; Rowland et al. 2024; Crespo Gómez et al. 2024, Hagimoto et al. in prep.).

Figure 3 shows the SEDs for the clumpy galaxy FL957 at $z = 7.7$. The left panel shows the SEDs for the four clumps, and the right panel shows the SEDs for the system-integrated and diffuse components. The dashed and solid lines represent intrinsic SEDs and dust-attenuated (with re-emission) SEDs, respectively.

From the SEDs, we calculate several dust properties as summarized in Table B.2: UV slope (β_{UV}), L_{IR} , L_{UV} , IRX, A_{UV} , and T_{peak} . The UV continuum slope β_{UV} is widely used as an indicator of UV continuum attenuation. Thanks to JWST’s unprecedented sensitivity in infrared imaging and spectroscopy extending up to $\lambda_{\text{obs}} \sim 5 \mu\text{m}$, robust measurements of the UV slope at $z \gtrsim 7$ have recently become available for the first time (e.g., Cullen et al. 2023; Topping et al. 2022; Morales et al. 2024; Cullen et al. 2024; Topping et al. 2024; Dottorini et al. 2024; Saxena et al. 2024). We calculate β_{UV} in the same way as in Liang et al. (2021b):

$$\beta_{\text{UV}} = \frac{\log_{10}(f_{\lambda, 1230\text{\AA}}) - \log_{10}(f_{\lambda, 3200\text{\AA}})}{\log_{10}(\lambda_{1230\text{\AA}}) - \log_{10}(\lambda_{3200\text{\AA}})}, \quad (2)$$

where $f_{\lambda, 1230\text{\AA}}$ and $f_{\lambda, 3200\text{\AA}}$ are the flux densities at rest-frame 1230\AA and 3200\AA , respectively. We adopt this wavelength range rather to avoid the UV bump effect at $\sim 2175 \text{\AA}$, which systematically leads to underestimations of the UV slope (Inoue et al. 2006; Narayanan et al. 2018b).

For the dust temperature, we calculate the peak dust temperature T_{peak} , which is obtained from the Wien displacement law from the rest-frame wavelength at which the infrared flux density (F_{ν}) peaks (λ_{peak})². This is defined as

$$T_{\text{d,peak}} = \frac{2.898 \times 10^3 \mu\text{m K}}{\lambda_{\text{peak}}}, \quad (3)$$

which follows the relation for a greybody with a dust emissivity index $\beta_{\text{d}} = 2$, i.e., $L_{\nu} \propto (1 - e^{-\tau_{\nu}})B_{\nu} \sim \nu^{\beta_{\text{d}}} B_{\nu} = \nu^{3+\beta_{\text{d}}} \frac{e^{h_{\nu}\nu/(k_{\text{B}}T)} - 1}{e^{h_{\nu}\nu/(k_{\text{B}}T)} - 1}$. This measure has been used in many observational studies (e.g., Casey et al. 2018; Schreiber et al. 2018; Burnham et al. 2021; Witstok et al. 2022; Mitsuhashi et al. 2024). Note that $T_{\text{d,peak}}$ is simply a proxy for λ_{peak} , and we adopt this definition for direct comparison with other theoretical and observational studies.

We define IRX as

$$\text{IRX} \equiv \frac{L_{\text{IR}}}{L_{\text{UV}}} = \frac{\int_{8 \mu\text{m}}^{1000 \mu\text{m}} L_{\lambda} d\lambda}{\lambda_{1600\text{\AA}} \circ L_{\lambda, 1600\text{\AA}}}, \quad (4)$$

where all wavelengths are in the rest frame.

We find that the intrinsic UV slope $\beta_{\text{UV},0}$ is almost the same for all components with $\beta_{\text{UV},0} = -2.8$ to -2.7 , but the attenuated β_{UV} is very different among components. In particular, Clumps 1 and 4 with large gas densities of $\sim 400\text{--}500 \text{ cm}^{-3}$ have large differences with $\Delta\beta = \beta_{\text{UV}} - \beta_{\text{UV},0} = 0.7, 1.0$, and the corresponding UV attenuation is also large with $A_{\text{UV}} \sim 2.95\text{--}4.60$. In contrast, the diffuse component has a very low gas density with a median value of $\langle n_{\text{gas}} \rangle = 1.9 \text{ cm}^{-3}$, and the attenuated slope is $\beta_{\text{UV}} = -2.35$ ($\Delta\beta = 0.35$) with $A_{\text{UV}} = 0.64$. This result is reflected in the system-integrated value, with a relatively blue

² The peak flux density is taken as B_{ν} , not B_{λ} .

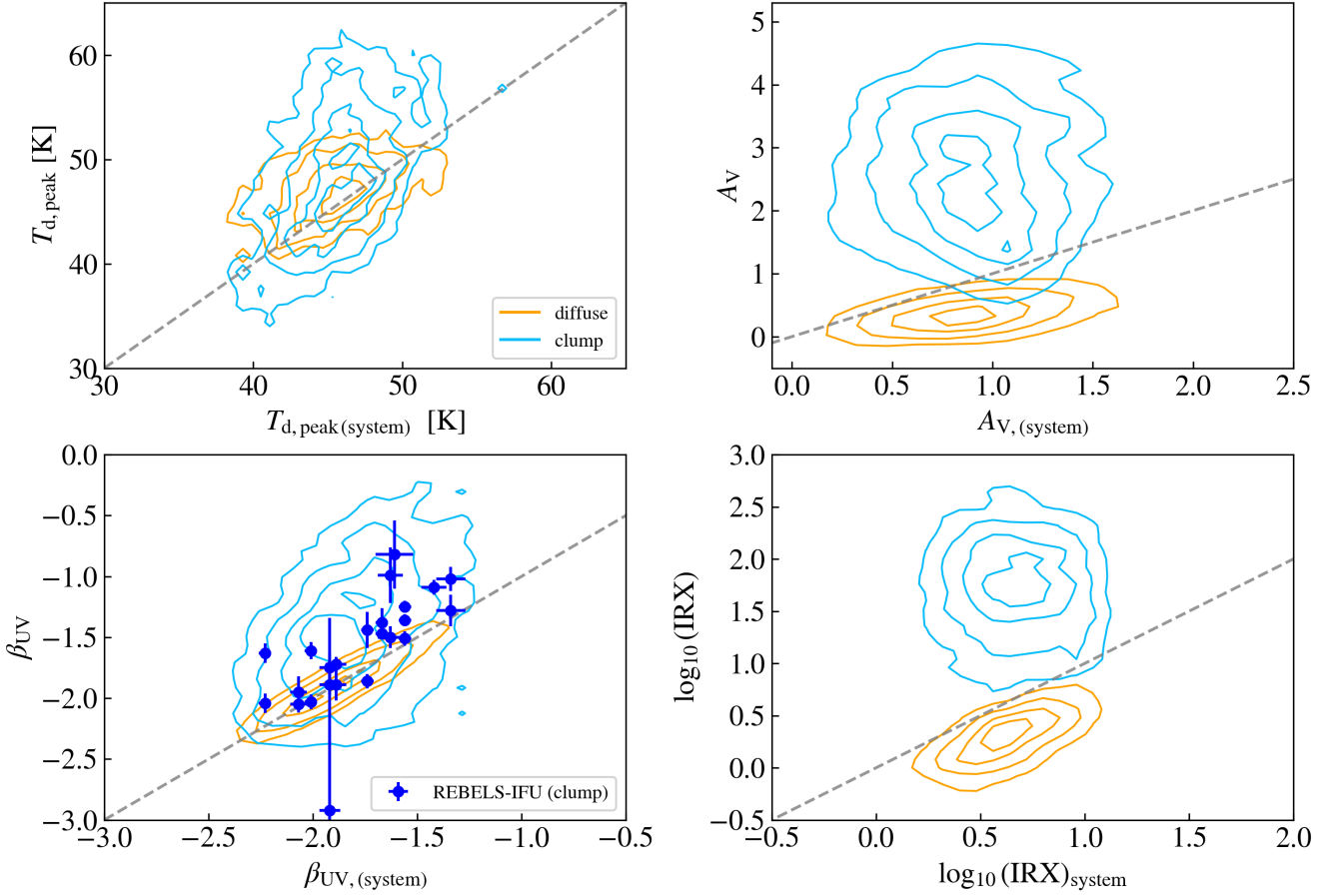


Figure 4. Comparison of dust properties between system-integrated values and individual components for all identified clumpy galaxies at $z = 6 - 9$. The x-axis of each panel shows the system-integrated value calculated over $10 \text{ kpc} \times 10 \text{ kpc}$ regions, while the y-axis shows values for individual clumps (cyan) and diffuse components (orange). Contours enclose 20%, 50%, 80%, and 95% of the data. *Top left:* peak dust temperature ($T_{\text{d,peak}}$). *Top right:* V-band attenuation (A_V). *Bottom left:* UV slope (β_{UV}). For comparison, we also plot observational results from the REBELS-IFU survey (Komarova et al. 2025; Fisher et al. 2025), comparing system-integrated and clump components. *Bottom right:* infrared excess ($\text{IRX} \equiv L_{\text{IR}}/L_{\text{UV}}$). The gray dashed line in each panel indicates the one-to-one relation.

slope of $\beta_{\text{UV}} = -2.34$. For the V-band attenuation A_V , clumps have large values ($A_V = 1.12 - 2.84$), while the diffuse and system components have $A_V = 0.09$ and 0.38 , respectively. We further discuss these values in terms of attenuation curves in Section 3.3.

For the dust peak temperature, we find that the four clumps in FL957 have temperatures 4–10 K higher than the diffuse component. This is because clumps have radiation sources in compact regions, and the dust temperature scales as $T_{\text{d}} \propto u_*^{1/(4+\beta_{\text{d}})} \sim (L_*/r^2)^{1/(4+\beta_{\text{d}})}$, where u_* , L_* , and r are the radiation energy density, luminosity of sources, and the distance between the radiation source and dust grains, respectively. Spatially resolved dust temperatures for $z \gtrsim 5$ galaxies (and quasars) have recently been investigated by high-resolution ALMA observations (e.g., Tsukui et al. 2023; Meyer et al. 2025; Villanueva et al. 2024; Fernández Aranda et al. 2025). In particular, the ALMA-CRISTAL survey found that the bridge regions between two clumps have 5 K

lower dust temperatures than the clumps, also showing similar trends.

Finally, for IRX , clumps have large values of $\log \text{IRX} = 0.68 - 1.99$, comparable to local (U)LIRGs (e.g., Goldader et al. 2002; Howell et al. 2010) and IR-selected dusty star-forming galaxies (DSFG) at $z \sim 2$ (Casey et al. 2014). They are up to around 2 dex larger than the diffuse and system components with $\log \text{IRX} = 0.07$ and 0.34 , respectively. We will further discuss this in terms of the $\text{IRX}-\Delta\beta$ relation in Section 4.2.

3.2. Dust properties: clumps vs system-integrated values

In the previous section, we have focused on the dust properties of individual clumps in FL957. In this section, we examine the statistical dust properties using all 376 clumpy galaxies identified in our simulations. Figure 4 shows various dust properties of the clump and diffuse components, plotted as a function of the corresponding system-integrated values.

Component	number	$\langle \beta_{\text{UV}} \rangle$	$\langle \beta_{\text{UV},0} \rangle$	$\langle \log_{10}(\text{IRX}) \rangle$	$\langle L_{\text{UV},1600} \rangle [L_{\odot}]$	$\langle L_{\text{IR}} \rangle [L_{\odot}]$	$\langle T_{\text{d,peak}} \rangle [\text{K}]$	$\langle A_{\text{UV}} \rangle$	$\langle A_{\text{V}} \rangle$	$\langle S \rangle$
Clump	1059	-1.47	-2.49	1.75	7.41×10^9	3.63×10^{11}	47.68	4.13	2.50	1.60
Diffuse	376	-1.90	-2.36	0.30	8.24×10^{11}	1.52×10^{12}	47.09	1.00	0.34	2.90
System	376	-1.88	-2.36	0.62	8.33×10^{11}	3.48×10^{12}	45.50	1.59	0.87	1.84

Table 1. Summary of median dust properties for clumpy galaxies identified in FirstLight simulations with a $40 \text{ cMpc}/h$ box at $z = 6\text{--}9.5$. We identified 376 clumpy systems containing 1059 clumps in total. Here, β_{UV} ($\beta_{\text{UV},0}$) is the UV slope for the attenuated (intrinsic) SED. Dust temperature is calculated as the peak dust temperature $T_{\text{d,peak}}$ (see Equation 3). The attenuation curve slope is defined as $S \equiv A_{\text{UV}}/A_{\text{V}}$. IRX is the infrared excess, defined as $\text{IRX} \equiv L_{\text{IR}}/L_{\text{UV}}$. Each value shows the median for each component. We categorize three components: clumps, diffuse regions, and system-integrated values.

We compare four key quantities: dust peak temperature, V-band attenuation, UV slope, and IRX.

The top-left panel shows that clumps exhibit larger scatter in dust temperature than the diffuse components and systematically show higher dust temperatures. Some clumps have $T_{\text{d,peak}} \sim 65 \text{ K}$, approximately 20 K higher than typical system-integrated values ($T_{\text{d,peak}} \sim 45 \text{ K}$), while the median values for clump and diffuse components are almost the same, $\sim 45\text{--}47 \text{ K}$ (see Table 1). These clumps with elevated dust temperatures reflect compact star formation regions, as discussed in Section 3.1.

For A_{V} in the top-right panel, clumps show large scatter and typically exhibit higher attenuation, with values up to 4 mag larger than the corresponding system-integrated values. In contrast, diffuse components lie systematically below the one-to-one line, with attenuation up to 0.7 mag lower than the system values. UV slopes in the bottom-left panel show similar trends: clumps have redder slopes with $\beta_{\text{UV,clump}} - \beta_{\text{UV,sys}}$ up to ~ 1 , while diffuse components have slopes similar to the system-integrated values. Recent JWST observations have begun to provide spatially resolved β_{UV} measurements using NIRCam photometry (e.g., Sugahara et al. 2025) and NIRSpec IFU spectroscopy (e.g., Marconcini et al. 2024; Komarova et al. 2025). For example, Fisher et al. (2025) and Komarova et al. (2025) reported system-integrated and clump-resolved β_{UV} values for 12 REBELS-IFU sample galaxies. From their measurements, we calculate clump-system differences of $\beta_{\text{UV,clump}} - \beta_{\text{UV,sys}} \simeq 0.2$ (up to 0.6; blue plots in the bottom-left panel of Figure 4), consistent with our simulation results.

For IRX in the bottom-right panel, clumps also exhibit large scatter and systematically show larger IRX values than the system-integrated values, with offsets up to ~ 2 dex. In contrast, diffuse components always have smaller IRX than the system values, with offsets up to ~ 0.5 dex. These distinct IRX distributions will be discussed in terms of the IRX- $\Delta\beta$ relation in Section 4.2. The mean values of these dust properties for each component are summarized in Table 1.

The large scatter and systematic offsets in dust properties between different components suggest that commonly used system-integrated measurements may not adequately represent the dust properties of individual star-forming regions. These component-level variations have important implications for interpreting spatially resolved observations and for

understanding the physical mechanisms governing dust attenuation and emission, which we explore in the following sections.

3.3. Attenuation curves

We investigate the dust attenuation curves for different components. The top panel of Figure 5 shows the attenuation curves for all identified clumpy galaxies, including individual clumps, diffuse components, and system-integrated values. The attenuation curves are derived from the SEDs, as exemplified for FL957 in Figure 3. The bottom panel shows the attenuation curve slope ($S \equiv A_{\text{UV}}/A_{\text{V}}$) versus V-band dust attenuation (A_{V}) for all components.

For the system-integrated attenuation curves (solid black lines), we find that they are grayer than the Calzetti attenuation curve (Calzetti et al. 2000), with a median slope of $\langle S \rangle = 1.84$. This trend toward grayer curves is consistent with recent JWST observations of $z \gtrsim 6$ galaxies (e.g., Markov et al. 2025; Shvai et al. 2025).

When we examine spatially resolved attenuation curves, however, we find significant variations among components. Clumps exhibit grayer (flatter) attenuation curves than the system-integrated curves, while diffuse components show much steeper curves. From the S - A_{V} relation (bottom panel), clumps systematically occupy the region with lower slopes (grayer curves) and higher A_{V} values, while diffuse components show higher slopes (steeper curves) with lower A_{V} values. The median slopes for clumps, diffuse components, and system-integrated values are $\langle S \rangle = 1.60, 2.90$, and 1.84, respectively (see also Table 1).

Similar trends of grayer curves in star-forming regions compared to system-integrated values have been observed in local galaxies (Chevallard et al. 2013; Decler et al. 2019; Matsumoto et al. 2026). However, these component-wise differences in EoR galaxies are quantitatively derived here for the first time. The physical origin of these systematic differences is discussed in Section 4.1.

4. DISCUSSION

4.1. Physical Origin of Component-wise Attenuation Curves

We have shown that our $z = 6\text{--}9$ galaxies exhibit grayer system-integrated attenuation curves than the Calzetti curve, with significant component-wise variations: clumps show the

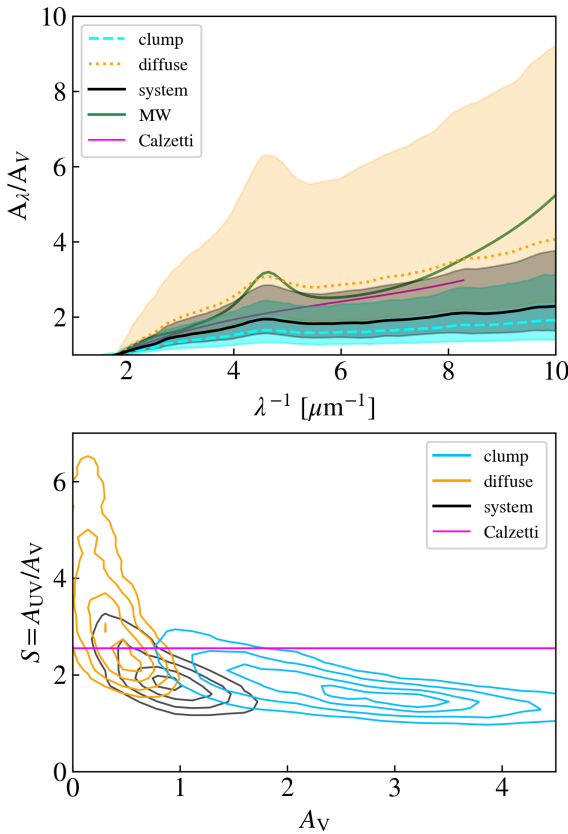


Figure 5. Top panel: Dust attenuation curves for the clumpy galaxies we identified in our simulations. The black solid line shows the median system-integrated attenuation curve, colored dashed lines show the median attenuation curves of individual clumps, and the orange dotted line shows the median of the diffuse component. Each shaded region shows the 5-95% range. For comparison, we plot the Calzetti attenuation curve (magenta [Calzetti et al. 2000](#)) and MW extinction curve (green [Cardelli et al. 1989](#)). Bottom panel: Attenuation curve slope ($S \equiv A_{\text{UV}}/A_V$) versus V-band dust attenuation (A_V) for all identified clumpy galaxies at $z = 6 - 9$. The black, cyan, and orange contours represent the system-integrated, individual clumps, and diffuse components, respectively. Contours enclose 20%, 50%, 80%, and 95% of the data. The horizontal magenta line indicates the Calzetti attenuation law.

grayest curves ($\langle S \rangle = 1.60$), while diffuse components show the steepest ($\langle S \rangle = 2.90$). We now investigate the physical origin of these systematic differences.

[Markov et al. \(2025\)](#) argue that grayer attenuation curves at high redshift compared to local galaxies can be reproduced by three factors: (i) larger A_V attenuation, (ii) larger dust grains, and (iii) compact dust-star geometry. For scenario (i), in regions with large dust attenuation (large A_V), dust absorption dominates over scattering processes, resulting in grayer attenuation curves (e.g., [Narayanan et al. 2018a](#); [Lin et al. 2021](#); [Matsumoto et al. 2026](#)). However, the S - A_V relation (Figure 5, bottom panel) shows that over 80% of our system-integrated curves are grayer than low- z ($z \sim 1-3$

star-forming galaxies at the same A_V ([Shivaei et al. 2025](#)). This indicates that scenario (i) is unlikely to be the dominant explanation. In scenario (ii), larger dust grains produce grayer extinction curves, leading to grayer attenuation curves. However, we adopt fixed dust compositions for MW-like dust ([Weingartner & Draine 2001](#)) (also SMC-like dust in Appendix C), and scenario (ii) does not apply to our study. Therefore, scenario (iii), compact dust-star geometry, is the most favored explanation for the grayer system-integrated curves. In our clumpy (i.e., extended) galaxies at $z = 6 - 9$, star-forming regions are compact and embedded in dense dusty environments, resulting in gray attenuation curves even at moderate A_V values.

The component-wise differences can be understood as a combination of scenarios (i) and (iii). Clumps exhibit grayer attenuation curves due to their higher optical depths, where dust absorption dominates over scattering, and their compact dust-star geometry. In these high optical depth environments, scattered photons are more likely to be absorbed before escaping, suppressing scattering effects and resulting in grayer curves ([Narayanan et al. 2018a](#)). In contrast, diffuse components have low optical depths, making scattering effects more pronounced. In optically thin regions, scattering can effectively reduce A_V while maintaining higher A_{UV} , resulting in steeper slopes (A_{UV}/A_V). The extended geometry of diffuse components also contributes to steeper curves.

In summary, clumps exhibit grayer attenuation curves due to their higher optical depths (i) and compact geometry (iii), where scattering effects are suppressed. Diffuse components, with their lower optical depths and extended geometries, show steeper curves dominated by scattering. In the next section, we use the $\text{IRX}-\Delta\beta$ relation to further distinguish qualitatively between the effects of optical depth and dust-star geometry. These systematic differences have important implications for interpreting spatially resolved dust observations and for accurate SED modeling of high-redshift clumpy galaxies.

4.2. Quantitative Evaluation of Dust-Star Geometry Using $\text{IRX}-\Delta\beta$

As shown by [Seon & Draine \(2016\)](#) and [Lin et al. \(2021\)](#), quantitatively evaluating the effects of both dust optical depth and dust-star geometry from attenuation curves alone is challenging. Because attenuation curves involve ratios of attenuations at different wavelengths, they are affected by the wavelength dependence of scattering. Properly accounting for photons scattered into the line of sight from outside requires full 3D radiative transfer calculations. However, the $\text{IRX}-\Delta\beta$ relation, where $\Delta\beta$ denotes the difference between the attenuated and intrinsic UV slopes, provides a more direct diagnostic of geometry and optical depth. When energy balance between absorbed UV and re-emitted IR radiation is approximately satisfied, the $\text{IRX}-\Delta\beta$ relation can be derived analytically as a function of dust optical depth and dust-star geometry. Following [Popping et al. \(2017\)](#) and [Lin et al. \(2021\)](#), we develop a toy model parameterized by only these two quantities.

We assume stellar and dust layers with scale heights H_* and H_d , respectively. The geometry is symmetric, and the dust layer has a uniform dust density, n_d . We define two key parameters: the dust-to-star scale-height ratio $R \equiv H_d/H_*$, and the fiducial optical depth

$$\tau_\lambda^{\text{fid}} = \sigma_\lambda n_d H_d, \quad (5)$$

where σ_λ is the dust cross-section, uniquely determined by the chosen dust extinction curve. We introduce the escape probability at wavelength λ as

$$P_{\text{esc},\lambda} \equiv L_{\text{obs},\lambda}/L_{\text{int},\lambda}, \quad (6)$$

where $L_{\text{obs},\lambda}$ and $L_{\text{int},\lambda}$ are the observed and intrinsic luminosities, respectively.

The dust geometry is categorized into four types based on the scale-height ratio R , as schematically illustrated in Figure 6. We assume that these geometries are symmetric about the midplane of the stellar distribution.

(i) $R = 0$: There is no dust layer, and therefore the observed luminosity equals the intrinsic luminosity, i.e., $P_{\text{esc},\lambda} = 1$.

(ii) $0 < R < 1$: This corresponds to the *sandwich* geometry (Xu & Buat 1995), with an escape probability given by

$$P_{\text{esc},\lambda} = \frac{1-R}{2}(1+e^{-\tau_\lambda^{\text{fid}}}) + \frac{R}{\tau_\lambda^{\text{fid}}}(1-e^{-\tau_\lambda^{\text{fid}}}). \quad (7)$$

(iii) $R = 1$: This corresponds to a well-mixed geometry, and the escape probability is given by

$$P_{\text{esc},\lambda} = \frac{1-e^{-\tau_\lambda^{\text{fid}}}}{\tau_\lambda^{\text{fid}}}. \quad (8)$$

Cases (ii) and (iii) can be considered as a continuous transition.

(iv) $R > 1$: This corresponds to a combination of well-mixed and screen geometries. The escape probability is then given by

$$P_{\text{esc},\lambda} = \frac{1-e^{-\tau_\lambda^{\text{mix}}}}{\tau_\lambda^{\text{mix}}} e^{-\tau_\lambda^{\text{screen}}}, \quad (9)$$

where we define optical depths for the well-mixed and screen components as

$$\tau_\lambda^{\text{mix}} = \sigma_\lambda n_d H_* = \sigma_\lambda n_d H_d \frac{H_*}{H_d} = \frac{\tau_\lambda^{\text{fid}}}{R}, \quad (10)$$

$$\tau_\lambda^{\text{screen}} = \sigma_\lambda n_d \frac{H_d - H_*}{2} = \frac{\tau_\lambda^{\text{fid}}}{2} \left(1 - \frac{1}{R}\right). \quad (11)$$

Next, we derive expressions for IRX and β_{UV} from this toy model. We introduce an effective optical depth defined as $\tau_{\text{eff},\lambda} = -\log_e(P_{\text{esc},\lambda})$. Assuming the intrinsic UV luminosity is balanced by the observed UV and re-emitted IR luminosities, IRX is expressed as

$$\text{IRX} = \frac{L_{\text{TIR}}}{L_{\text{obs},\text{UV}}} = \frac{1-e^{-\tau_{\text{eff},\text{UV}}}}{e^{-\tau_{\text{eff},\text{UV}}}} = \frac{1-P_{\text{esc},\text{UV}}}{P_{\text{esc},\text{UV}}}. \quad (12)$$

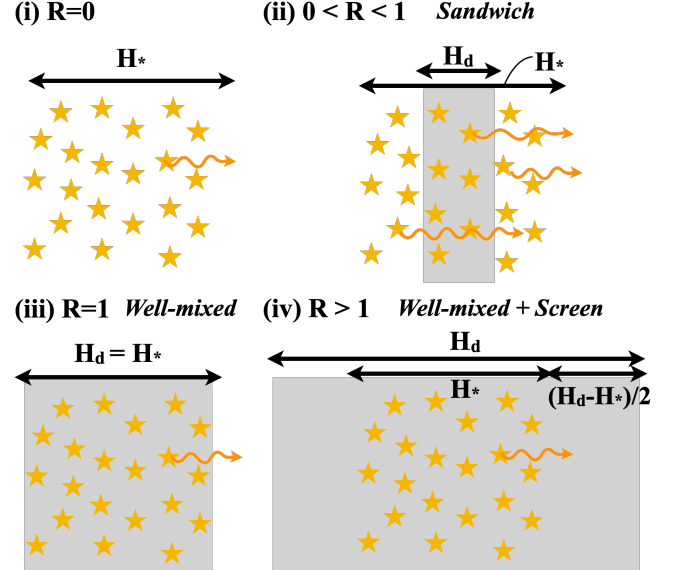


Figure 6. Illustration of the four simplified dust-star geometry models characterized by different dust-to-star scale height ratios ($R \equiv H_d/H_*$). Stars represent the stellar layer with scale height H_* , and gray shaded areas indicate the uniform dust layer with scale height H_d . Orange arrows schematically represent escaping UV radiation. The escape probability for each geometry type is derived explicitly in the main text.

We adopt a wavelength of 1600 Å as representative of UV radiation.

To define the UV slope, we select two wavelengths consistent with Section 3.1: $\lambda_1 = 1230$ Å and $\lambda_2 = 3200$ Å. The observed UV slope is then

$$\begin{aligned} \beta_{\text{UV}} &= \frac{\log_{10}(f_{\lambda_1}) - \log_{10}(f_{\lambda_2})}{\log_{10}(\lambda_1) - \log_{10}(\lambda_2)} \\ &= \frac{\log_{10}(f_{\lambda_1}^0) - \log_{10}(f_{\lambda_2}^0) - (\log_{10} e) \times (\tau_{\text{eff},\lambda_1} - \tau_{\text{eff},\lambda_2})}{\log_{10}(\lambda_1) - \log_{10}(\lambda_2)} \\ &= \frac{\log_{10}(f_{\lambda_1}^0) - \log_{10}(f_{\lambda_2}^0)}{\log_{10}(\lambda_1) - \log_{10}(\lambda_2)} + \frac{-0.43(\tau_{\text{eff},\lambda_1} - \tau_{\text{eff},\lambda_2})}{\log_{10}(\lambda_1) - \log_{10}(\lambda_2)} \\ &= \beta_{\text{UV},0} + \Delta\beta, \end{aligned} \quad (13)$$

where f_λ (f_λ^0) denotes the observed (intrinsic) flux density at wavelength λ .

Finally, we derive the fiducial optical depth at $\lambda = \lambda_1$ as

$$\tau_{\lambda_1}^{\text{fid}} = \tau_{\text{UV}}^{\text{fid}} \left(\frac{A_{\lambda_1}}{A_{\text{UV}}} \right), \quad (14)$$

where the attenuation ratio is uniquely set by the adopted extinction curve. The intrinsic UV slope $\beta_{\text{UV},0}$ depends on the intrinsic SED, specifically stellar population age (star formation history) and metallicity. According to Eq. (13), $\Delta\beta$ is independent of the intrinsic SED and depends only on the dust geometry, provided that the dust type is fixed. We therefore use $\Delta\beta$ in the following analysis.

We construct theoretical grids on the $\text{IRX}-\Delta\beta$ plane by parameterizing dust-star geometry through R and the fiducial optical depth $\tau_{\text{UV}}^{\text{fid}}$. Figure 7 shows $\text{IRX}-\Delta\beta$ grids obtained by varying these two parameters.

In the case of $R = 0$, the position on the $\text{IRX}-\Delta\beta$ plane is fixed at $(\Delta\beta, \text{IRX}) = (0, 0)$. As $R \rightarrow 0$, the toy model represents a scenario with a very thin dust sheet placed symmetrically at the center of the stellar distribution. In the optically thick regime ($\tau_{\text{UV}}^{\text{fid}} \gg 1$), radiation from behind this central dust sheet is absorbed and re-emitted in the IR, whereas radiation from the front side escapes directly as UV emission. These two contributions become equal, causing IRX to asymptotically approach unity. This $\text{IRX} \sim 1$ limit represents a limitation of the idealized symmetric geometry and is not realized in actual clumps. For $0 < R < 1$, the grid curves exhibit a characteristic inverted-C shape because escaping radiation includes reddened contributions from the obscured backside. When $R = 1$ (fully well-mixed), the UV slope remains nearly constant at $\Delta\beta \simeq -\log_e(\tau_{\lambda_1}^{\text{fid}}/\tau_{\lambda_2}^{\text{fid}})/\log_e(\lambda_1/\lambda_2)$ as the optical depth increases ($\tau_{\text{UV}}^{\text{fid}} \gtrsim 1$), and IRX increases vertically. For large R values ($R \gtrsim 3$), the geometry approaches a screen model as shown by the solid black line.

In simulations, intrinsic physical properties such as the intrinsic UV slope ($\beta_{\text{UV},0}$) are readily available for each component, and the dust type can be consistently fixed (MW-type dust is assumed throughout Figure 7). In what follows, we therefore utilize the $\text{IRX}-\Delta\beta$ plane to interpret the dust geometry in our simulated galaxies.

Figure 7 shows our simulated galaxies on the $\text{IRX}-\Delta\beta$ plane, enabling direct interpretation of dust-star geometry³. From this figure, we find that clumps occupy the region with $\tau_{\text{UV}}^{\text{fid}} \gtrsim 10$ and $R \simeq 1$, indicating well-mixed geometry. System-integrated values have $\tau_{\text{UV}}^{\text{fid}} \sim 3\text{--}20$ and $R \simeq 0.8$, exhibiting sandwich geometries. Diffuse components have small fiducial optical depths ($\tau_{\text{UV}}^{\text{fid}} \lesssim 10$), making geometry determinations difficult.

In terms of optical depth (i.e., dust column density), clumps have ~ 10 times larger column densities than the system-integrated values (with extreme cases up to ~ 100 times). Despite their large optical depths, the escape probability for well-mixed geometry scales as $P_{\text{esc,UV}} \propto \tau_{\text{UV}}^{\text{fid}}{}^{-1}$, allowing a small fraction of UV photons to escape. These high optical depths result from gas compression during interactions with companion galaxies, significantly enhancing local dust column densities.

We also plot observational results of system-integrated $z \sim 7$ galaxies obtained from the REBELS-IFU survey as gray circles in Figure 7. We adopt IRX results from Bowler et al. (2024) and $\Delta\beta$ from Fisher et al. (2025). Here, $\Delta\beta$ is

³ We note that our toy model assumes component-wise energy balance. This assumption is well-justified for compact clumps with small surface areas, where external UV contributions are negligible. For extended diffuse components, deviations from strict energy balance may occur, though the qualitative trends remain valid.

obtained using flexible attenuation curve fitting. These data points are located in similar regions to the system-integrated values in our simulation results.

To interpret the dust-star geometry more quantitatively, we extract the corresponding $(R, \tau_{\text{UV}}^{\text{fid}})$ combinations from their positions on the $\text{IRX}-\Delta\beta$ plane. The left panel of Figure 8 shows how different components map onto the toy-model parameter space. Clumps have a median of $R = 1.0$, with scatter systematically extending toward $R > 1$, and high optical depths with median $\log_{10} \tau_{\text{UV}}^{\text{fid}} \sim 1.6$. System-integrated values have $R < 1$ with median $\log_{10} \tau_{\text{UV}}^{\text{fid}} \sim 0.85$.

To validate these toy-model-inferred values, we directly calculated the dust-star geometry parameters from our simulations. While defining scale heights for extended components is challenging, we measured the half-mass radius ratio between dust and stars for compact clumps, finding values of $r_d/r_* \sim 1$ (corresponding to $R \sim 1$), consistent with the well-mixed interpretation. The directly calculated fiducial optical depths for clumps, derived from dust column density maps, span $\log_{10} \tau_{\text{UV}}^{\text{fid}} \sim 1.5\text{--}2.0$ (median ~ 1.9), in reasonable agreement with the toy-model-inferred median of ~ 1.6 . This consistency validates that the toy model successfully captures the dust-star geometry of our simulated galaxies.

We also apply this framework to the observed REBELS-IFU galaxies (system-integrated) and find that most samples span $R \lesssim 1$ and $\log_{10} \tau_{\text{UV}}^{\text{fid}} \sim 0.5\text{--}1.5$, consistent with the system-integrated values in our simulated galaxies. The right panel of Figure 8 schematically illustrates these results: star-forming clumps (~ 100 pc scale) have ~ 1 dex larger column densities than the system average and exhibit well-mixed geometries, while system-integrated values represent a mixture of clumps and weakly attenuated diffuse components, interpreted as sandwich geometry in the 1D toy model.

In summary, given a known dust type (extinction curve), the $\text{IRX}-\Delta\beta$ plane effectively diagnoses dust-star geometry, distinguishing between the effects of optical depth and geometric configuration. Recent JWST observations have enabled the derivation of attenuation curves, which will allow future observations to derive intrinsic UV slopes and $\Delta\beta$, ultimately enabling quantitative decomposition of these effects using this diagnostic plane.

4.3. Implications for Spatially Resolved Observations

Our spatially resolved analysis of dust absorption and re-emission properties reveals systematic variations that have important implications for interpreting observations of high-redshift galaxies.

First, we find that dust temperatures vary spatially (Figure 4), with clump peak temperatures up to $\Delta T_{\text{d,peak}} \sim 20$ K higher than system-integrated values. Such temperature variations reflect differences in local heating sources and dust column densities. While direct spatially resolved dust temperature measurements require high-resolution multi-band IR observations that remain challenging (Villanueva et al. 2024), alternative methods using spatially resolved UV continuum with single-band IR observations (Inoue et al. 2020;

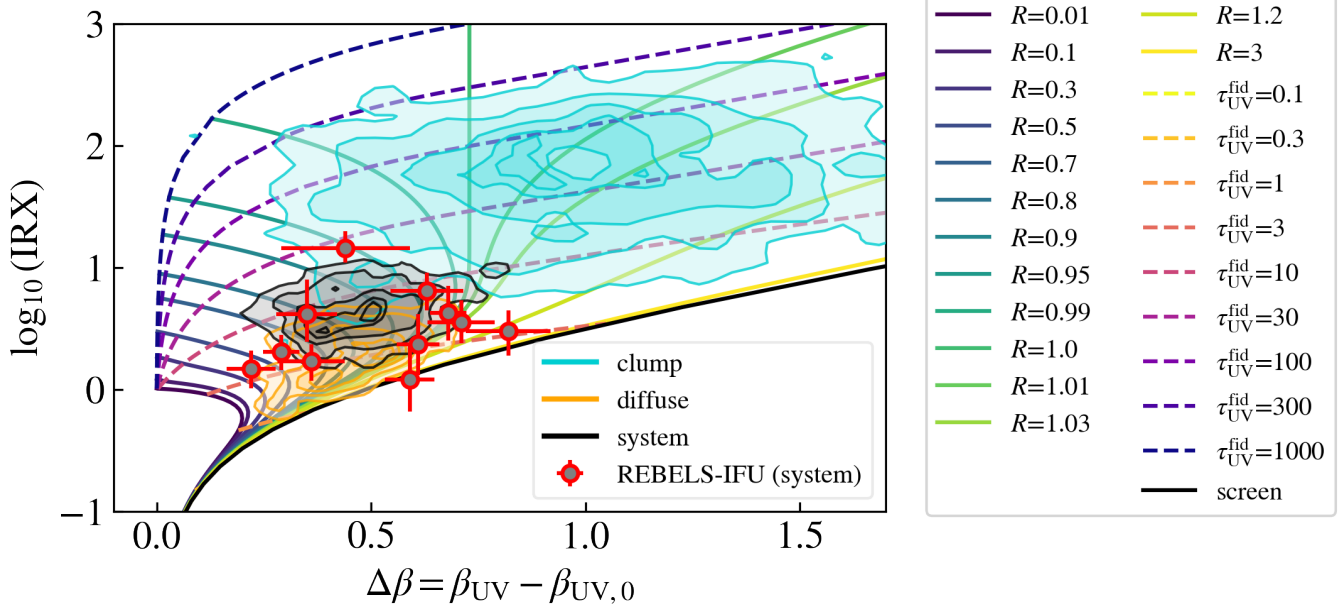


Figure 7. IRX– $\Delta\beta$ relation with toy model predictions, where $\Delta\beta \equiv \beta_{\text{UV}} - \beta_{\text{UV},0}$ represents the change in UV slope due to dust attenuation. We show theoretical curves for different combinations of the dust-to-star scale-height ratio (R) and fiducial UV optical depth ($\tau_{\text{UV}}^{\text{fid}}$), which parametrize the dust-star geometry and dust column density, respectively. The solid black lines represent the limiting case of a foreground screen geometry ($R \gg 1$). Contours show our simulation results for the clumpy, diffuse, and system-integrated components at $z = 6–9$; black for the system-integrated value, cyan for the individual clumps, and orange for the diffuse component. Contours enclose 20%, 50%, 80%, and 95% of the data. All simulation data assume MW-type dust properties, and the toy model grids are calculated using the MW extinction curve with $R_V = 3.1$ (Cardelli et al. 1989). For comparison, we plot the REBELS-IFU (system-integrated) data from Fisher et al. (2025) and Bowler et al. (2024).

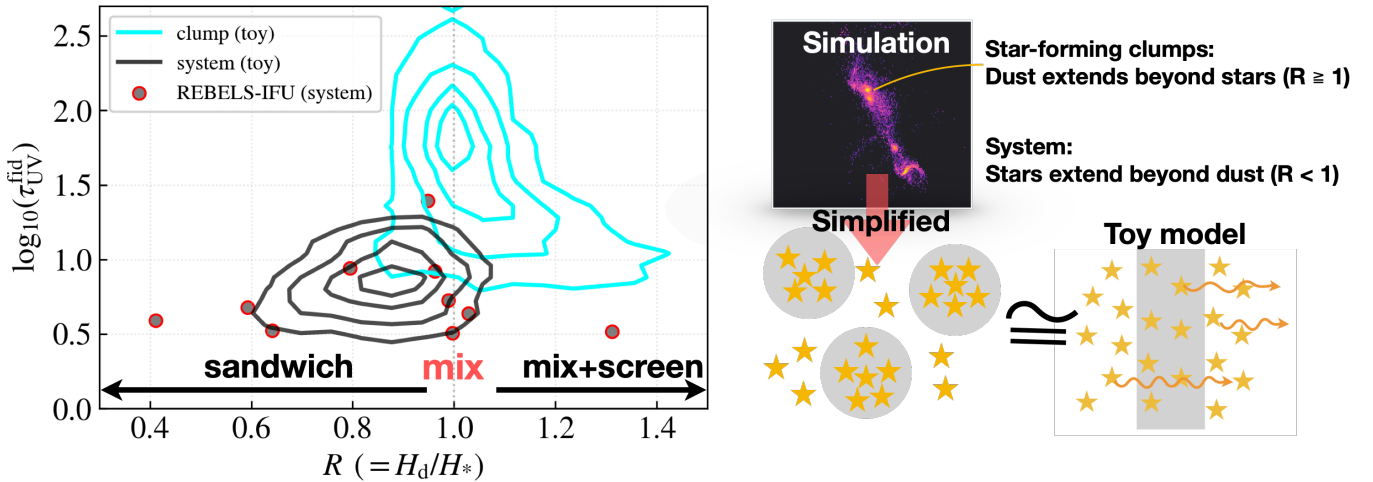


Figure 8. Left: Distributions of the dust-to-star scale-height ratio (R) and fiducial UV optical depth ($\tau_{\text{UV}}^{\text{fid}}$) for clump components (cyan) and system-integrated values (black). These contours and the gray circles show values inferred from the toy-model grid matching in Figure 7, where the latter represents the REBELS-IFU (system-integrated) data. The contours enclose 20%, 50%, 80%, and 95% of the data. Right: Schematic illustration connecting the spatial structure of simulated galaxies to the toy model framework: clumpy regions exhibit dust-extended or co-spatial dust/stellar distributions ($R \geq 1$) with ~ 1 dex larger dust column densities than system-averaged, while system-integrated values represent the stellar-extended geometry due to diffuse components ($R < 1$).

Fudamoto et al. 2023) or [CII] emission lines (Sommovigo et al. 2021) offer promising avenues for future studies. Such measurements would enable direct comparison with our predictions and provide constraints on the spatial distribution of heating sources (e.g., young stellar populations, evolved stars, AGN) and dust masses within high-redshift galaxies.

Second, variations in attenuation curves directly affect pixel-by-pixel SED fitting (Figure 5). Recent JWST NIR-Cam observations have enabled pixel-by-pixel SED fitting of high-redshift galaxies (e.g., Giménez-Arteaga et al. 2023, 2024). However, these studies typically assume a fixed attenuation law (often Calzetti) for all pixels. Our results show that star-forming clumps have grayer attenuation curves than the Calzetti law, while diffuse regions (tails and bridges) have steeper curves.

If a fixed Calzetti law is applied to all pixels, systematic biases arise. For clumps with grayer curves, the Calzetti law (which is steeper) will underestimate A_V . To reproduce the observed UV colors with lower A_V , SED fitting will favor younger stellar populations with intrinsically bluer colors and lower mass-to-light ratios, leading to underestimated stellar masses. Conversely, for diffuse components with steeper curves, the Calzetti law (which is shallower) will overestimate A_V , favoring older populations with higher mass-to-light ratios and leading to overestimated stellar masses.

While the impact of attenuation curve variations on integrated galaxy stellar mass estimates has been studied (e.g., Lo Faro et al. 2017; Pforr et al. 2012), our work is the first to investigate these effects on spatially resolved scales within individual galaxies. Recent studies have begun using flexible attenuation curve models to characterize system-integrated properties in JWST observations (Markov et al. 2025; Shivaai et al. 2025; Fisher et al. 2025) and deriving intrinsic UV slopes (Fisher et al. 2025). Our results suggest that such flexible parametrizations should also be applied at the pixel-by-pixel level, allowing attenuation curves to vary spatially within individual galaxies rather than adopting a single curve for the entire system.

Such spatially varying attenuation curves would enable the derivation of intrinsic UV slopes at each spatial location. Combined with spatially resolved IRX measurements, this would allow us to construct spatially resolved IRX– $\Delta\beta$ maps and thereby probe the dust-star geometry and optical depth on sub-galactic scales. Although only a handful of studies have derived spatially resolved IRX for $z \gtrsim 5$ galaxies (Sugahara et al. 2025; Lines et al. 2025; Mawatari et al. 2025; Bakx et al. 2025), we expect such observations to become increasingly available with future JWST/ALMA programs.

4.4. Caveats

There are several caveats to our study. First, we adopt a fixed dust-to-metal ratio of 0.4. According to Dayal et al. (2022), DTM keeps the constant value of 0.37 when considering only stellar-path production. However, in reality, processes such as astration and destruction act to reduce the DTM, while ejection (which preferentially removes gas-phase metals) and grain growth act to increase it. More-

over, the efficiency of grain growth depends on the accretion timescale for gas-phase metals to stick onto dust grains, which scales as $t_{\text{acc}} \propto n^{-1} T^{-1/2} Z^{-1}$. The equation implies that higher-density, lower-temperature, higher-metallicity environments such as molecular clouds favor collisions and subsequent sticking between gas-phase metals and grains (Dwek 1998; Zhukovska et al. 2008). In future work we will therefore implement a fully time-dependent DTM obtained from semi-analytic models (e.g., Dayal et al. 2022; Tsuna et al. 2023; Toyouchi et al. 2025) and cosmological simulations (e.g., Aoyama et al. 2017; Graziani et al. 2020; Kannan et al. 2025).

Second, we assume a fixed dust composition and size distribution: Milky Way- and SMC-like mixtures. The high-redshift dust is believed to form predominantly in core-collapse supernovae (Mancini et al. 2015) and to be processed by shocks in such a way that small grains are preferentially destroyed, biasing the population toward larger particles (Makiya & Hirashita 2022; Narayanan et al. 2025b). Because grains with radii exceeding the photon wavelength scatter and absorb nearly independently of wavelength (Mie 1908), a distribution dominated by large grains produces a gray (flat) attenuation curve. Exploring evolving dust yields, shattering, coagulation, and ISM growth in a self-consistent framework that allows both composition and size distribution to vary with redshift is a natural next step for future investigations.

Third, we identify clumps based on star-formation rate (SFR) densities, a method that physically targets gravitationally bound structures. In practice, however, the definition of a “clump” and the choice of aperture size vary significantly across observational studies. If an observational aperture is larger than our model-defined clump scale, it may incorporate the surrounding diffuse component, resulting in a lower IRX that approaches galaxy-integrated values. Therefore, our results should be viewed as a conservative characterization of the intrinsic properties of the clump structures themselves, representing the high-density limit of these systems. Creating realistic mock observations that include noise and PSF effects, and identifying clumps based on flux rather than SFR density (e.g., Punyasheel et al. 2025, Ceverino et al. in prep.), would facilitate a more direct comparison with observations.

5. SUMMARY AND CONCLUSIONS

We present spatially resolved dust properties, including dust temperature, UV slope, attenuation curves, and infrared excess (IRX), for clumpy galaxies ($M_* \simeq 10^{8-10} M_\odot$) at $z = 6-9$ using cosmological zoom-in simulations. By performing post-processing dust radiative transfer calculations, we obtain pixel-by-pixel SEDs for each simulated galaxy. We identify star-forming giant clumps ($R \gtrsim 100$ pc, $\text{SFR} \gtrsim 1 M_\odot \text{ yr}^{-1}$) based on SFR surface density, detecting 376 clumpy systems and 1059 individual clumps in total at $z = 6-9$. For each clumpy system, we analyze three components: clumps, diffuse regions, and system-integrated values, and statistically compare their dust properties.

We find that clumps exhibit systematically higher $T_{\text{d,peak}}$, A_{V} , A_{UV} , and redder β_{UV} compared to system-integrated values, with large scatter. In contrast, diffuse components show similar $T_{\text{d,peak}}$ and β_{UV} but smaller A_{V} and A_{UV} than system-integrated values, with much smaller scatter. Some clumps have temperatures up to 20 K higher than their host galaxies' system-integrated values. The median IRX of clumps is 1–2 dex larger than both diffuse and system-integrated values, indicating dramatically different dust obscuration levels within individual galaxies.

For attenuation curves, we find that system-integrated values for our simulated galaxies are grayer than the Calzetti law. For spatially resolved results, we find that clumps have grayer attenuation curves than the system-integrated values, while diffuse components exhibit much steeper curves due to enhanced scattering effects in optically thin regions. Even though our post-processing dust model assumes MW-like (or SMC-like) dust, we obtain grayer curves, implying that optical depth and dust-star geometry are the main contributors to this shallowness.

To decompose these two factors, we develop a toy model that utilizes the IRX– $\Delta\beta$ plane, where $\Delta\beta$ is the difference between the attenuated and intrinsic UV slopes. This model characterizes dust properties using two parameters: dust optical depth ($\tau_{\text{UV}}^{\text{fid}}$, i.e., dust column density) and the dust-to-star scale-height ratio (R). We find that clumps have ~ 10 times higher dust column densities than system-integrated values and exhibit co-spatial or dust-extended geometries, while system-integrated values show star-extended geometries due to contributions from optically thin diffuse components. Comparison with REBELS-IFU observations shows that observed $z \sim 7$ galaxies have dust properties consistent with our system-integrated values.

These results have important implications for interpreting spatially resolved observations of high-redshift galaxies. Pixel-by-pixel measurements of attenuation curves will be crucial for accurately determining physical properties from

SED fitting. Furthermore, as clump-by-clump IRX– $\Delta\beta$ measurements become available, they will enable direct constraints on dust-star geometry and optical depth. Such spatially resolved observations are becoming feasible, particularly in gravitationally lensed systems (e.g., VENUS survey, JWST GO-6882). While our analysis focuses on high-redshift clumpy galaxies, the methodology and findings are equally applicable to spatially resolved observations at lower redshifts (e.g., HIDING survey, ALMA Cycle 12 large program).

The combination of next-generation spatially resolved observations from JWST and ALMA with detailed radiative transfer modeling will be essential for understanding the physical conditions in individual star-forming regions and for accurately characterizing dust properties across cosmic time.

6. ACKNOWLEDGEMENTS

YN thank Masato Hagimoto, Amiel Sternberg, and Rachel Somerville, Irene Shvarei, Masami Ouchi, Kartheik Iyer, and Laura Sommovigo for fruitful discussion. This work made use of v2.3 of the Binary Population and Spectral Synthesis (BPASS) models as described in [Byrne et al. \(2022\)](#) and [Stanway & Eldridge \(2018\)](#). Numerical computations and analyses were carried out on the Cray XD2000 and the analysis servers at Center for Computational Astrophysics, National Astronomical Observatory of Japan. YN acknowledges funding from JSPS KAKENHI Grant Number 23KJ0728, a JSR fellowship, and Flatiron Research Fellowship. The Flatiron Institute is a division of the Simons Foundation. AKI is supported by JSPS KAKENHI Grant Number 23H00131. TH acknowledges financial support from the JSPS (19KK0353) and the Kyoto University Foundation. DC is supported by research grant PID2021-122603NB-C21 funded by the Ministerio de Ciencia, Innovación y Universidades (MICIU/FEDER), project PID2024-156100NB-C21 financed by MICIU/AEI /10.13039/501100011033 / FEDER, EU., and the research grant CNS2024-154550 funded by MICIU/AEI/10.13039/501100011033.

APPENDIX

A. NUMERICAL CONVERGENCE AND ADDITIONAL PHYSICAL PROCESSES

In this appendix, we check the numerical convergence of our RT simulations and the effects of stochastic heating and self-absorption. Table A.1 summarizes our test calculation. Here, n_p denotes the number of photon packets launched per wavelength grid point, and n_λ denotes the number of grid points used for the wavelength grid. By default, we use $(n_p, n_\lambda) = (10^7, 150)$. By default, we use $(n_p, n_\lambda) = (10^7, 150)$.

In Figure A.1, we show the SEDs for $(n_p, n_\lambda) = (10^8, 150)$ and $(10^7, 300)$. The differences from the default case are less than 2 percent across most wavelength regions in the rest-UV and rest-FIR. Such small differences are negli-

gible when integrated over observed photometric filters, confirming that our results are numerically converged.

Additionally, we also plot a case without stochastic heating, i.e., the assumption that all grains are in thermal equilibrium with the incident radiation field. The SED plotted in blue lacks the rest mid-IR emission, which are emitted from very small grains such as PAH. They underestimate re-emission flux from stochastic heating by up to a factor of two. Such rest-frame mid-IR windows overlaps well with the spectral range of the proposed PRIMA instrument ([Mouillet et al. 2023, 2025](#)), making it a crucial probe for distinguishing the effects of stochastic heating in these high- z galaxies.

The green line is an SED without self-absorption of dust, and it shows a net decrease of flux both in the mid-IR and FIR. Without self-absorption, the re-absorption and subse-

name	n_p	n_λ	self-absorption	stochastic heating
fiducial	10^7	150	○	○
nw300	10^7	300	○	○
np1e8	10^8	150	○	○
LTE	10^7	150	○	×
w/o self-absorption	10^7	150	×	○

Table A.1. The parameters used in each SKIRT calculation in Appendix A. All cases adopt MW-like dust type (Weingartner & Draine 2001) and fixed dust-to-metal ratio of 0.4. Here, n_p is the number of photon packets launched per wavelength grid point, and n_λ is the number of wavelength grid points.

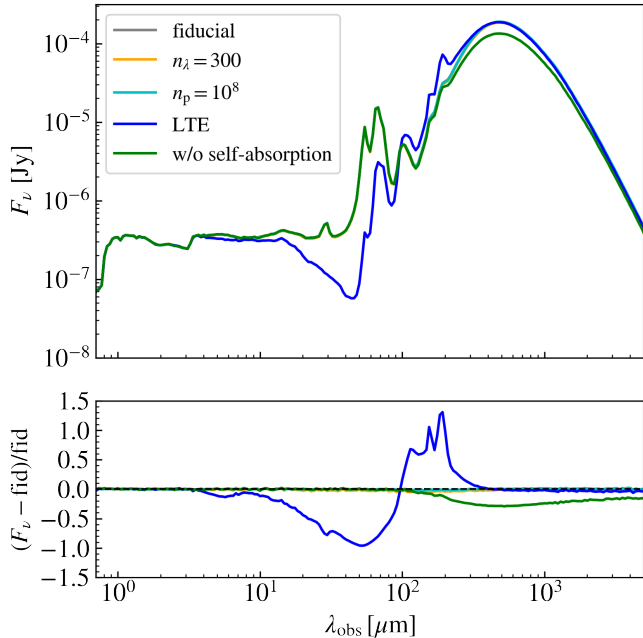


Figure A.1. SEDs of FL957 at $z = 7.7$ computed with different SKIRT settings. In the upper panel, we plot the SED for the fiducial case and two runs with more wavelength bins ($n_\lambda = 300$), and more photon packages ($n_p = 10^8$) launched per wavelength bin. Additionally, we show the outcome of simulations for which stochastic heating or self-absorption is turned off (“LTE”, “w/o self-absorption”). The detailed SKIRT settings in each model are described in Table A.1. In the lower panel, we show the fractional difference between the various runs and the fiducial model.

quent re-emission of dust radiation within optically thick regions are not accounted for, leading to an underestimation of IR flux. Consequently, the flux can be underestimated by up to 25% with respect to the fiducial simulation.

B. PHYSICAL PROPERTIES OF THE CLUMPY GALAXY FL957 AT $Z = 7.7$

In Section 3.1, we present a detailed case study of FL957 at $z = 7.7$. Tables B.1 and B.2 summarize the physical and dust properties for each component (clumps, diffuse, and system-integrated) of this galaxy.

C. THE CASE OF SMC-LIKE DUST

In the main text, we investigated dust properties such as $T_{d,peak}$, A_V , attenuation curves, and $\text{IRX}-\Delta\beta$ assuming MW-like dust. In this Appendix, we examine the case of SMC-like dust to test the robustness of our results to different dust compositions.

Figure C.1 shows the comparison of dust properties between system-integrated values and individual components (clumps and diffuse regions) for SMC-like dust. Since the SMC extinction curve is steeper than the MW curve at rest-frame UV wavelengths and lacks a UV bump, the UV slope β_{UV} is shifted redder by $\langle\beta_{\text{UV,SMC}}\rangle - \langle\beta_{\text{UV,MW}}\rangle \sim 0.3-0.7$ (see the bottom-left panel of Figure C.1 and Table C.1). However, the median values and scatter from the system-integrated values for other properties such as peak dust temperature and attenuation (A_V , A_{UV}) are similar to those of MW-like dust.

Figure C.2 shows dust attenuation curves for SMC-like dust. Although the dust composition differs, the attenuation curves for system-integrated values are similar to those of MW-like dust: grayer than the Calzetti attenuation law with $\langle S_{\text{Cal}} \rangle - \langle S_{\text{SMC(MW)}} \rangle = 0.5 (0.7)$. The behavior that attenuation curves for clumps (diffuse components) are grayer (steeper) than the system-integrated curves remains the same as in the MW case.

For the $\text{IRX}-\Delta\beta$ relations, we plot them in Figure C.3, respectively. The toy model grids introduced in Section 4.2 are calculated using the SMC extinction curve. Since the $\text{IRX}-\Delta\beta$ relation depends only on geometry and dust column density for a fixed dust composition, the locations of clumps, diffuse components, and system-integrated values occupy the same coordinates in the $(R, \tau_{\text{UV}}^{\text{fid}})$ parameter space as in the MW case⁴.

In summary, while the choice of dust composition (MW vs. SMC) affects the absolute values of UV slopes due to differences in extinction curve shapes, the relative differences between clumps, diffuse regions, and system-integrated values remain consistent. Our main conclusions regarding the spatial variations of dust properties and their physical interpretation via the toy model are robust to the choice of dust composition.

⁴ Although the dust mass opacity κ_{UV} at 1600 Å differs slightly between MW and SMC dust models (7.45×10^4 and $8.25 \times 10^4 \text{ cm}^2 \text{ g}^{-1}$, respectively; Weingartner & Draine 2001), this $\sim 10\%$ difference results in nearly identical positions in the $(R, \tau_{\text{UV}}^{\text{fid}})$ parameter space.

Component	$M_{*,\text{all}}$ [M_{\odot}]	$M_{*,\text{young}}$ [M_{\odot}]	Age_{mw} [Myr]	$\langle n_{\text{gas}} \rangle$ [cm^{-3}]	Σ_{SFR} [$M_{\odot} \text{ yr}^{-1} \text{ kpc}^{-2}$]	SFR [$M_{\odot} \text{ yr}^{-1}$]	sSFR [Gyr^{-1}]	R_{clump} [pc]
Clump 1	3.21×10^8	8.05×10^7	39	492	115	8.1	25.1	149
Clump 2	3.63×10^7	2.37×10^7	26	345	59	2.4	65.2	113
Clump 3	1.93×10^8	4.63×10^7	34	191	71	4.6	24.0	144
Clump 4	1.32×10^8	8.26×10^7	30	400	107	8.3	62.7	157
Diffuse	2.72×10^9	4.25×10^8	100	1.9	-	42.5	15.6	-
System	3.40×10^9	6.58×10^8	87	2.8	-	65.8	19.4	-

Table B.1. Summary of physical properties of FL957 at $z = 7.70$, which contains four clumps within a $10 \times 10 \text{ kpc}^2$ region. $M_{*,\text{young}}$ refers to stellar masses younger than 10 Myr, and $M_{*,\text{all}}$ refers to stellar masses for all ages. Clump age (Age_{mw}) is calculated as the mass-weighted stellar age within the clump. The clump radius R_{clump} is obtained as $R_{\text{clump}} = \sqrt{\Delta^2 N_{\text{grid}} / \pi}$, where Δ is the pixel size and N_{grid} is the number of pixels within the clump.

Component	β_{UV}	$\beta_{\text{UV},0}$	$\log_{10}(\text{IRX})$	$L_{\text{UV},1600} [\text{L}_{\odot}]$	$L_{\text{IR}} [\text{L}_{\odot}]$	$T_{\text{d,peak}} [\text{K}]$	A_{UV}	A_V	$S = A_{\text{UV}}/A_V$
Clump 1	-1.68	-2.76	1.99	5.59×10^9	5.51×10^{11}	55.0	4.60	2.84	1.62
Clump 2	-2.30	-2.80	0.68	1.94×10^{10}	9.33×10^{10}	57.4	1.75	1.12	1.56
Clump 3	-2.49	-2.78	0.94	3.03×10^{10}	2.61×10^{11}	52.7	2.21	1.58	1.40
Clump 4	-2.11	-2.85	1.29	2.34×10^{10}	4.57×10^{11}	52.7	2.95	1.68	1.76
Diffuse	-2.35	-2.70	0.07	1.16×10^{12}	1.36×10^{12}	48.3	0.64	0.09	6.79
System	-2.34	-2.74	0.34	1.23×10^{12}	2.69×10^{12}	52.7	1.02	0.38	2.69

Table B.2. Summary of dust properties for FL957 at $z = 7.70$ (same system as in Table B.1). Dust properties are defined as in Table 1.

Component	number	$\langle \beta_{\text{UV}} \rangle$	$\langle \beta_{\text{UV},0} \rangle$	$\langle \log_{10}(\text{IRX}) \rangle$	$\langle L_{\text{UV},1600} \rangle [\text{L}_{\odot}]$	$\langle L_{\text{IR}} \rangle [\text{L}_{\odot}]$	$\langle T_{\text{d,peak}} \rangle [\text{K}]$	$\langle A_{\text{UV}} \rangle$	$\langle A_V \rangle$	$\langle S \rangle$
Clump	1059	-0.74	-2.49	1.8	7.38×10^9	4.23×10^{11}	48.04	4.24	2.36	1.75
Diffuse	376	-1.59	-2.38	0.27	7.97×10^{11}	1.41×10^{12}	47.04	0.94	0.35	3.69
System	376	-1.56	-2.37	0.59	8.12×10^{11}	3.24×10^{12}	46.52	1.50	0.76	1.99

Table C.1. Summary of median dust properties for clumpy galaxies, as the same as Table 1.

REFERENCES

Abdurro'uf, Coe, D., Jung, I., et al. 2023, ApJ, 945, 117, doi: [10.3847/1538-4357/acba06](https://doi.org/10.3847/1538-4357/acba06)

Algera, H. S. B., Inami, H., Sommovigo, L., et al. 2024, MNRAS, 527, 6867, doi: [10.1093/mnras/stad3111](https://doi.org/10.1093/mnras/stad3111)

Aoyama, S., Hou, K.-C., Shimizu, I., et al. 2017, MNRAS, 466, 105, doi: [10.1093/mnras/stw3061](https://doi.org/10.1093/mnras/stw3061)

Baes, M., Verstappen, J., De Looze, I., et al. 2011, ApJS, 196, 22, doi: [10.1088/0067-0049/196/2/22](https://doi.org/10.1088/0067-0049/196/2/22)

Bakx, T. J. L. C., Sommovigo, L., Tamura, Y., et al. 2025, arXiv e-prints, arXiv:2511.08327, doi: [10.48550/arXiv.2511.08327](https://doi.org/10.48550/arXiv.2511.08327)

Behrens, C., Pallottini, A., Ferrara, A., Gallerani, S., & Vallini, L. 2018, MNRAS, 477, 552, doi: [10.1093/mnras/sty552](https://doi.org/10.1093/mnras/sty552)

Bowler, R. A. A., Cullen, F., McLure, R. J., Dunlop, J. S., & Avison, A. 2022, MNRAS, 510, 5088, doi: [10.1093/mnras/stab3744](https://doi.org/10.1093/mnras/stab3744)

Bowler, R. A. A., Inami, H., Sommovigo, L., et al. 2024, MNRAS, 527, 5808, doi: [10.1093/mnras/stad3578](https://doi.org/10.1093/mnras/stad3578)

Burnham, A. D., Casey, C. M., Zavala, J. A., et al. 2021, ApJ, 910, 89, doi: [10.3847/1538-4357/abe401](https://doi.org/10.3847/1538-4357/abe401)

Byrne, C. M., Stanway, E. R., Eldridge, J. J., McSwiney, L., & Townsend, O. T. 2022, MNRAS, 512, 5329, doi: [10.1093/mnras/stac807](https://doi.org/10.1093/mnras/stac807)

Calzetti, D., Armus, L., Bohlin, R. C., et al. 2000, ApJ, 533, 682, doi: [10.1086/308692](https://doi.org/10.1086/308692)

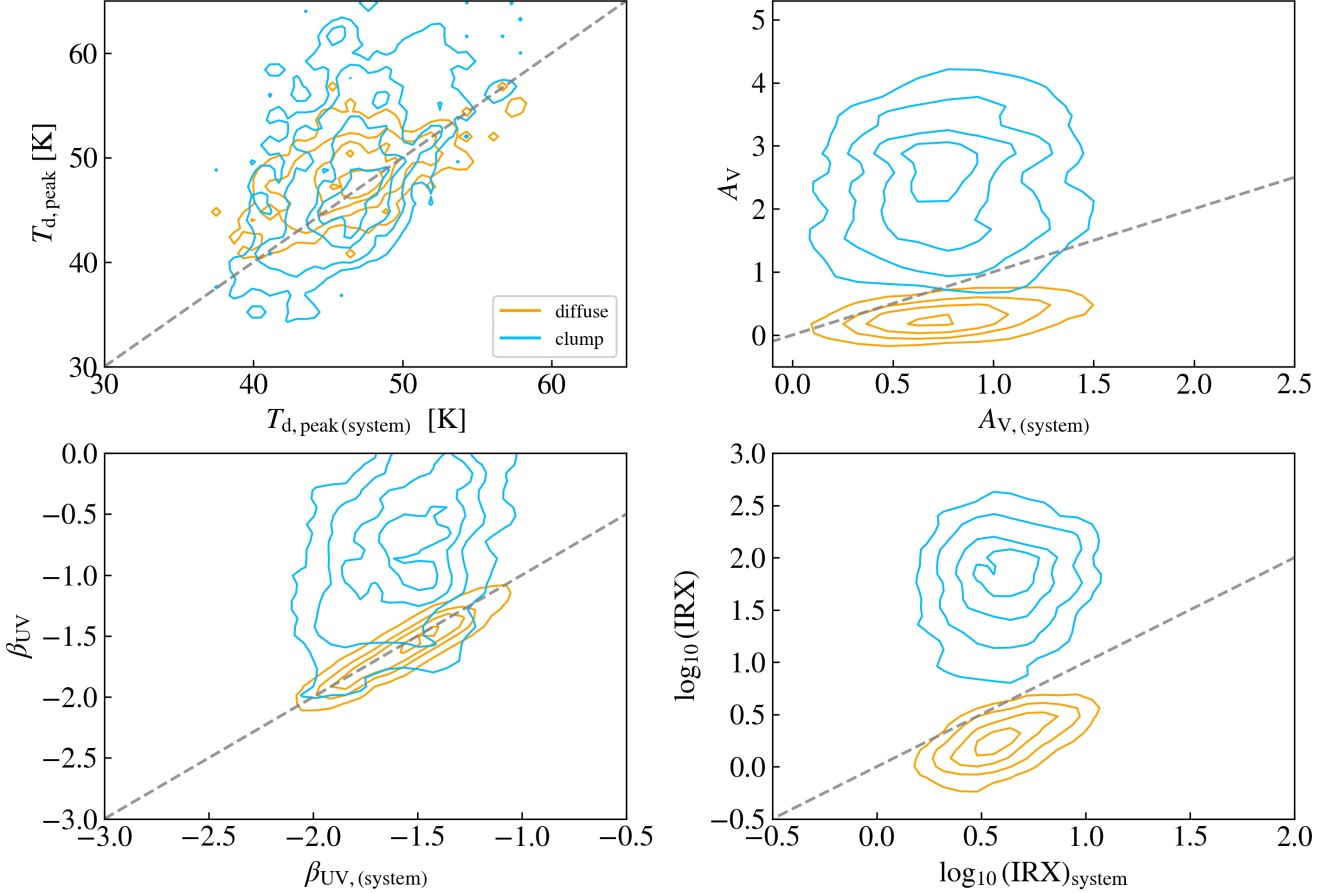


Figure C.1. Comparison of dust properties between system-integrated values and individual components for all identified clumpy galaxies at $z = 6 - 9$ as the same as Figure 4.

Calzetti, D., Kinney, A. L., & Storchi-Bergmann, T. 1994, ApJ, 429, 582, doi: [10.1086/174346](https://doi.org/10.1086/174346)

Cameron, A. J., Katz, H., Witten, C., et al. 2024, MNRAS, 534, 523, doi: [10.1093/mnras/stae1547](https://doi.org/10.1093/mnras/stae1547)

Camps, P., & Baes, M. 2015, Astronomy and Computing, 9, 20, doi: [10.1016/j.ascom.2014.10.004](https://doi.org/10.1016/j.ascom.2014.10.004)

—. 2020, Astronomy and Computing, 31, 100381, doi: [10.1016/j.ascom.2020.100381](https://doi.org/10.1016/j.ascom.2020.100381)

Cardelli, J. A., Clayton, G. C., & Mathis, J. S. 1989, ApJ, 345, 245, doi: [10.1086/167900](https://doi.org/10.1086/167900)

Casey, C. M., Scoville, N. Z., Sanders, D. B., et al. 2014, ApJ, 796, 95, doi: [10.1088/0004-637X/796/2/95](https://doi.org/10.1088/0004-637X/796/2/95)

Casey, C. M., Zavala, J. A., Spilker, J., et al. 2018, ApJ, 862, 77, doi: [10.3847/1538-4357/aac82d](https://doi.org/10.3847/1538-4357/aac82d)

Cataldi, P., Pedrosa, S., Pellizza, L. J., Ceverino, D., & Bignone, L. A. 2025, arXiv e-prints, arXiv:2510.05299, doi: [10.48550/arXiv.2510.05299](https://doi.org/10.48550/arXiv.2510.05299)

Ceverino, D., Dekel, A., & Bournaud, F. 2010, MNRAS, 404, 2151, doi: [10.1111/j.1365-2966.2010.16433.x](https://doi.org/10.1111/j.1365-2966.2010.16433.x)

Ceverino, D., Glover, S. C. O., & Klessen, R. S. 2017, MNRAS, 470, 2791, doi: [10.1093/mnras/stx1386](https://doi.org/10.1093/mnras/stx1386)

Ceverino, D., Hirschmann, M., Klessen, R. S., et al. 2021, MNRAS, 504, 4472, doi: [10.1093/mnras/stab1206](https://doi.org/10.1093/mnras/stab1206)

Ceverino, D., Klessen, R. S., & Glover, S. C. O. 2018, MNRAS, 480, 4842, doi: [10.1093/mnras/sty2124](https://doi.org/10.1093/mnras/sty2124)

—. 2019, MNRAS, 484, 1366, doi: [10.1093/mnras/stz079](https://doi.org/10.1093/mnras/stz079)

Ceverino, D., & Klypin, A. 2009a, ApJ, 695, 292, doi: [10.1088/0004-637X/695/1/292](https://doi.org/10.1088/0004-637X/695/1/292)

—. 2009b, ApJ, 695, 292, doi: [10.1088/0004-637X/695/1/292](https://doi.org/10.1088/0004-637X/695/1/292)

Ceverino, D., Klypin, A., Klimek, E. S., et al. 2014, MNRAS, 442, 1545, doi: [10.1093/mnras/stu956](https://doi.org/10.1093/mnras/stu956)

Ceverino, D., Nakazato, Y., Yoshida, N., Klessen, R. S., & Glover, S. C. O. 2024, A&A, 689, A244, doi: [10.1051/0004-6361/202450224](https://doi.org/10.1051/0004-6361/202450224)

Chen, Z., Stark, D. P., Endsley, R., et al. 2023, MNRAS, 518, 5607, doi: [10.1093/mnras/stac3476](https://doi.org/10.1093/mnras/stac3476)

Chevallard, J., Charlot, S., Wandelt, B., & Wild, V. 2013, MNRAS, 432, 2061, doi: [10.1093/mnras/stt523](https://doi.org/10.1093/mnras/stt523)

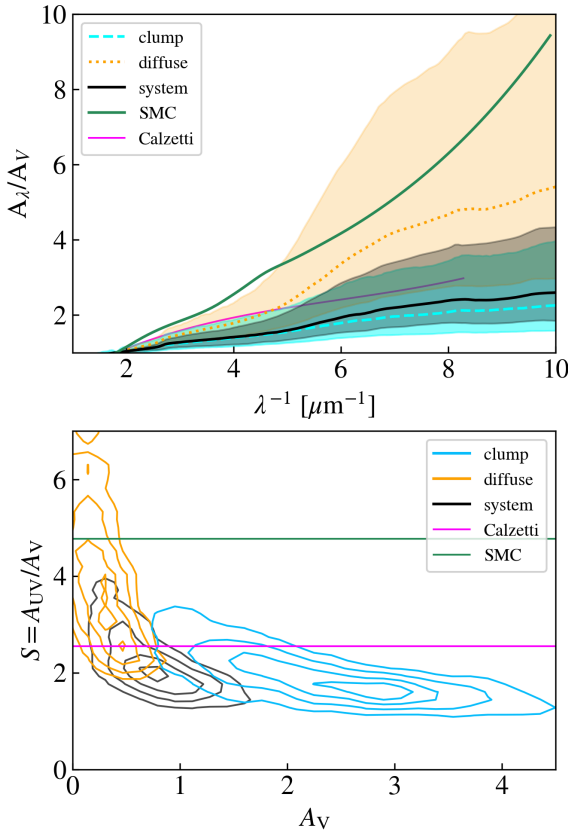


Figure C.2. Dust attenuation curves (top panel) and attenuation curve slope ($S \equiv A_{\text{UV}}/A_V$) versus V-band dust attenuation (A_V) for all identified clumpy galaxies at $z = 6 - 9$ (bottom panel) as the same as Figure 5. The SMC extinction curve is adopted from Gordon et al. (2003).

Crespo Gómez, A., Colina, L., Álvarez-Márquez, J., et al. 2024, *A&A*, 691, A325, doi: [10.1051/0004-6361/202449750](https://doi.org/10.1051/0004-6361/202449750)

Cullen, F., McLure, R. J., McLeod, D. J., et al. 2023, *MNRAS*, 520, 14, doi: [10.1093/mnras/stad073](https://doi.org/10.1093/mnras/stad073)

Cullen, F., McLeod, D. J., McLure, R. J., et al. 2024, *MNRAS*, 531, 997, doi: [10.1093/mnras/stae1211](https://doi.org/10.1093/mnras/stae1211)

da Cunha, E., Walter, F., Smail, I. R., et al. 2015, *ApJ*, 806, 110, doi: [10.1088/0004-637X/806/1/110](https://doi.org/10.1088/0004-637X/806/1/110)

Dayal, P., Ferrara, A., Sommovigo, L., et al. 2022, *MNRAS*, 512, 989, doi: [10.1093/mnras/stac537](https://doi.org/10.1093/mnras/stac537)

Decleir, M., De Looze, I., Boquien, M., et al. 2019, *MNRAS*, 486, 743, doi: [10.1093/mnras/stz805](https://doi.org/10.1093/mnras/stz805)

Dome, T., Tacchella, S., Fialkov, A., et al. 2024, *MNRAS*, 527, 2139, doi: [10.1093/mnras/stad3239](https://doi.org/10.1093/mnras/stad3239)

Dottorini, D., Calabro, A., Pentericci, L., et al. 2024, *arXiv e-prints*, arXiv:2412.01623, doi: [10.48550/arXiv.2412.01623](https://doi.org/10.48550/arXiv.2412.01623)

Draine, B. T., Aniano, G., Krause, O., et al. 2014, *ApJ*, 780, 172, doi: [10.1088/0004-637X/780/2/172](https://doi.org/10.1088/0004-637X/780/2/172)

Dwek, E. 1998, *ApJ*, 501, 643, doi: [10.1086/305829](https://doi.org/10.1086/305829)

Eldridge, J. J., Stanway, E. R., Xiao, L., et al. 2017, *PASA*, 34, e058, doi: [10.1017/pasa.2017.51](https://doi.org/10.1017/pasa.2017.51)

Ferland, G. J., Korista, K. T., Verner, D. A., et al. 1998, *PASP*, 110, 761, doi: [10.1086/316190](https://doi.org/10.1086/316190)

Fernández Aranda, R., Díaz Santos, T., Hatziminaoglou, E., et al. 2025, *A&A*, 695, L15, doi: [10.1051/0004-6361/202453214](https://doi.org/10.1051/0004-6361/202453214)

Fisher, R., Bowler, R. A. A., Stefanon, M., et al. 2025, *MNRAS*, 539, 109, doi: [10.1093/mnras/staf485](https://doi.org/10.1093/mnras/staf485)

Fudamoto, Y., Inoue, A. K., & Sugahara, Y. 2023, *MNRAS*, 521, 2962, doi: [10.1093/mnras/stad743](https://doi.org/10.1093/mnras/stad743)

Giménez-Arteaga, C., Oesch, P. A., Brammer, G. B., et al. 2023, *ApJ*, 948, 126, doi: [10.3847/1538-4357/acc5ea](https://doi.org/10.3847/1538-4357/acc5ea)

Giménez-Arteaga, C., Fujimoto, S., Valentino, F., et al. 2024, *A&A*, 686, A63, doi: [10.1051/0004-6361/202349135](https://doi.org/10.1051/0004-6361/202349135)

Goldader, J. D., Meurer, G., Heckman, T. M., et al. 2002, *ApJ*, 568, 651, doi: [10.1086/339165](https://doi.org/10.1086/339165)

Gordon, K. D., Clayton, G. C., Misselt, K. A., Landolt, A. U., & Wolff, M. J. 2003, *ApJ*, 594, 279, doi: [10.1086/376774](https://doi.org/10.1086/376774)

Graziani, L., Schneider, R., Ginolfi, M., et al. 2020, *MNRAS*, 494, 1071, doi: [10.1093/mnras/staa796](https://doi.org/10.1093/mnras/staa796)

Haardt, F., & Madau, P. 1996, *ApJ*, 461, 20, doi: [10.1086/177035](https://doi.org/10.1086/177035)

Hahn, O., & Abel, T. 2011, *MNRAS*, 415, 2101, doi: [10.1111/j.1365-2966.2011.18820.x](https://doi.org/10.1111/j.1365-2966.2011.18820.x)

Hainline, K. N., Johnson, B. D., Robertson, B., et al. 2024, *ApJ*, 964, 71, doi: [10.3847/1538-4357/ad1ee4](https://doi.org/10.3847/1538-4357/ad1ee4)

Harikane, Y., Inoue, A. K., Ellis, R. S., et al. 2025, *ApJ*, 980, 138, doi: [10.3847/1538-4357/ad9b2c](https://doi.org/10.3847/1538-4357/ad9b2c)

Howell, J. H., Armus, L., Mazzarella, J. M., et al. 2010, *ApJ*, 715, 572, doi: [10.1088/0004-637X/715/1/572](https://doi.org/10.1088/0004-637X/715/1/572)

Inami, H., Algera, H. S. B., Schouws, S., et al. 2022, *MNRAS*, 515, 3126, doi: [10.1093/mnras/stac1779](https://doi.org/10.1093/mnras/stac1779)

Inoue, A. K. 2011, *MNRAS*, 415, 2920, doi: [10.1111/j.1365-2966.2011.18906.x](https://doi.org/10.1111/j.1365-2966.2011.18906.x)

Inoue, A. K., Buat, V., Burgarella, D., et al. 2006, *MNRAS*, 370, 380, doi: [10.1111/j.1365-2966.2006.10499.x](https://doi.org/10.1111/j.1365-2966.2006.10499.x)

Inoue, A. K., Hashimoto, T., Chihara, H., & Koike, C. 2020, *MNRAS*, 495, 1577, doi: [10.1093/mnras/staa1203](https://doi.org/10.1093/mnras/staa1203)

Ishikawa, Y., Zakamska, N. L., Shen, Y., et al. 2025, *ApJ*, 982, 22, doi: [10.3847/1538-4357/adb4ee](https://doi.org/10.3847/1538-4357/adb4ee)

Kannan, R., Puchwein, E., Smith, A., et al. 2025, *arXiv e-prints*, arXiv:2502.20437, doi: [10.48550/arXiv.2502.20437](https://doi.org/10.48550/arXiv.2502.20437)

Katz, H., Cameron, A. J., Saxena, A., et al. 2025, *The Open Journal of Astrophysics*, 8, 104, doi: [10.33232/001c.142570](https://doi.org/10.33232/001c.142570)

Kennicutt, Robert C., J. 1998, *ARA&A*, 36, 189, doi: [10.1146/annurev.astro.36.1.189](https://doi.org/10.1146/annurev.astro.36.1.189)

Komarova, L., Stefanon, M., Laza-Ramos, A., et al. 2025, *arXiv e-prints*, arXiv:2511.10743, doi: [10.48550/arXiv.2511.10743](https://doi.org/10.48550/arXiv.2511.10743)

Kravtsov, A. V. 2003, *ApJL*, 590, L1, doi: [10.1086/376674](https://doi.org/10.1086/376674)

Kravtsov, A. V., Klypin, A. A., & Khokhlov, A. M. 1997, *ApJS*, 111, 73, doi: [10.1086/313015](https://doi.org/10.1086/313015)

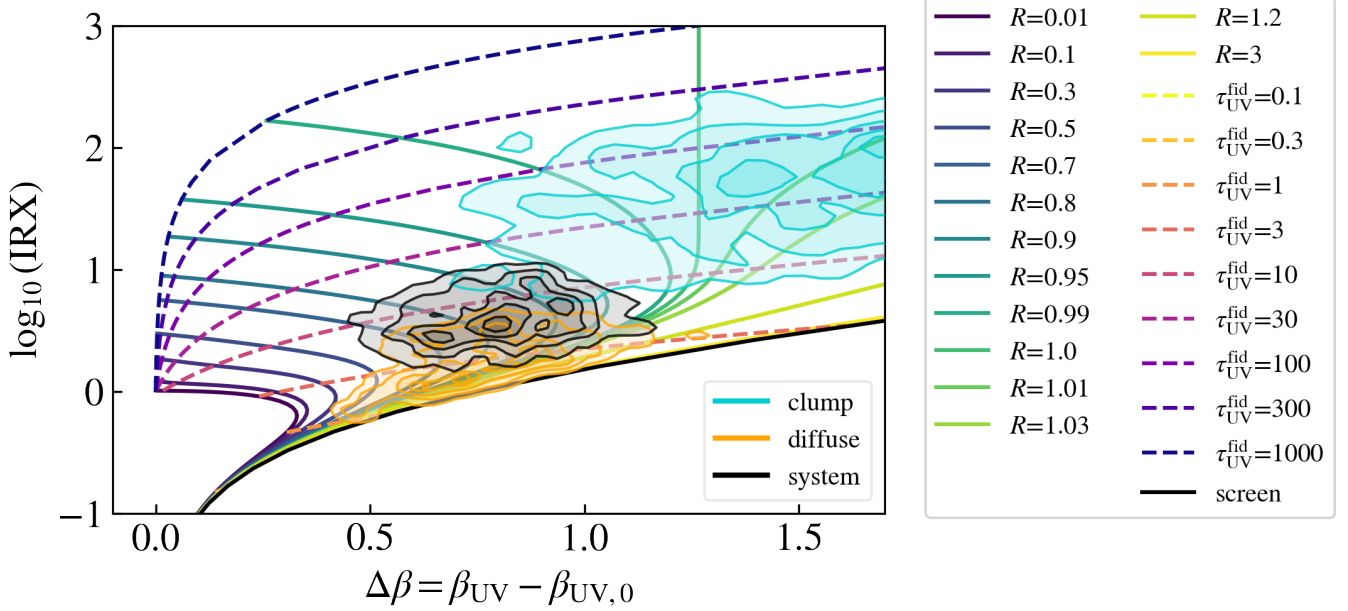


Figure C.3. IRX– $\Delta\beta$ relation with toy model predictions, where $\Delta\beta \equiv \beta_{\text{UV}} - \beta_{\text{UV},0}$ represents the change in UV slope due to dust attenuation, as the same as Figure 7.

Langan, I., Ceverino, D., & Finlator, K. 2020, MNRAS, 494, 1988, doi: [10.1093/mnras/staa880](https://doi.org/10.1093/mnras/staa880)

Li, Q., Yang, X. J., & Li, A. 2024, MNRAS, 535, L58, doi: [10.1093/mnrasl/slae095](https://doi.org/10.1093/mnrasl/slae095)

Liang, L., Feldmann, R., Hayward, C. C., et al. 2021a, MNRAS, 502, 3210, doi: [10.1093/mnras/stab096](https://doi.org/10.1093/mnras/stab096)

—. 2021b, MNRAS, 502, 3210, doi: [10.1093/mnras/stab096](https://doi.org/10.1093/mnras/stab096)

Liang, L., Feldmann, R., Kereš, D., et al. 2019, MNRAS, 489, 1397, doi: [10.1093/mnras/stz2134](https://doi.org/10.1093/mnras/stz2134)

Lin, Q., Yang, X., Li, A., & Witstok, J. 2025, A&A, 694, A84, doi: [10.1051/0004-6361/202452372](https://doi.org/10.1051/0004-6361/202452372)

Lin, Y.-H., Hirashita, H., Camps, P., & Baes, M. 2021, MNRAS, 507, 2755, doi: [10.1093/mnras/stab2242](https://doi.org/10.1093/mnras/stab2242)

Lines, N. E. P., Bowler, R. A. A., Adams, N. J., et al. 2025, MNRAS, 539, 2685, doi: [10.1093/mnras/staf627](https://doi.org/10.1093/mnras/staf627)

Lo Faro, B., Buat, V., Roehlly, Y., et al. 2017, MNRAS, 472, 1372, doi: [10.1093/mnras/stx1901](https://doi.org/10.1093/mnras/stx1901)

Lovell, C. C., Geach, J. E., Davé, R., Narayanan, D., & Li, Q. 2021, MNRAS, 502, 772, doi: [10.1093/mnras/staa4043](https://doi.org/10.1093/mnras/staa4043)

Makiya, R., & Hirashita, H. 2022, MNRAS, 517, 2076, doi: [10.1093/mnras/stac2762](https://doi.org/10.1093/mnras/stac2762)

Mancini, M., Schneider, R., Graziani, L., et al. 2015, MNRAS, 451, L70, doi: [10.1093/mnrasl/slv070](https://doi.org/10.1093/mnrasl/slv070)

Marconcini, C., D'Eugenio, F., Maiolino, R., et al. 2024, MNRAS, 533, 2488, doi: [10.1093/mnras/stae1971](https://doi.org/10.1093/mnras/stae1971)

Markov, V., Gallerani, S., Ferrara, A., et al. 2025, Nature Astronomy, 9, 458, doi: [10.1038/s41550-024-02426-1](https://doi.org/10.1038/s41550-024-02426-1)

Markov, V., Gallerani, S., Pallottini, A., et al. 2023, A&A, 679, A12, doi: [10.1051/0004-6361/202346723](https://doi.org/10.1051/0004-6361/202346723)

Matsumoto, K., Sommovigo, L., Gebek, A., et al. 2026, A&A, 705, A75, doi: [10.1051/0004-6361/202555658](https://doi.org/10.1051/0004-6361/202555658)

Mawatari, K., Costantin, L., Usui, M., et al. 2025, arXiv e-prints, arXiv:2507.02053, doi: [10.48550/arXiv.2507.02053](https://doi.org/10.48550/arXiv.2507.02053)

Meurer, G. R., Heckman, T. M., & Calzetti, D. 1999, ApJ, 521, 64, doi: [10.1086/307523](https://doi.org/10.1086/307523)

Meyer, R. A., Walter, F., Di Mascia, F., et al. 2025, A&A, 695, L18, doi: [10.1051/0004-6361/202453279](https://doi.org/10.1051/0004-6361/202453279)

Mie, G. 1908, Annalen der Physik, 330, 377, doi: [10.1002/andp.19083300302](https://doi.org/10.1002/andp.19083300302)

Mitsuhashi, I., Harikane, Y., Bauer, F. E., et al. 2024, ApJ, 971, 161, doi: [10.3847/1538-4357/ad5675](https://doi.org/10.3847/1538-4357/ad5675)

Morales, A. M., Finkelstein, S. L., Leung, G. C. K., et al. 2024, ApJL, 964, L24, doi: [10.3847/2041-8213/ad2de4](https://doi.org/10.3847/2041-8213/ad2de4)

Mouillet, A., Kataria, T., Lis, D., et al. 2023, arXiv e-prints, arXiv:2310.20572, doi: [10.48550/arXiv.2310.20572](https://doi.org/10.48550/arXiv.2310.20572)

Mouillet, A., Burgarella, D., Kataria, T., et al. 2025, arXiv e-prints, arXiv:2511.10927, doi: [10.48550/arXiv.2511.10927](https://doi.org/10.48550/arXiv.2511.10927)

Mushtaq, M., Ceverino, D., Klessen, R. S., Reissl, S., & Puttasiddappa, P. H. 2023, MNRAS, 525, 4976, doi: [10.1093/mnras/stad2602](https://doi.org/10.1093/mnras/stad2602)

Nakazato, Y., Ceverino, D., & Yoshida, N. 2024, ApJ, 975, 238, doi: [10.3847/1538-4357/ad7d0b](https://doi.org/10.3847/1538-4357/ad7d0b)

Nakazato, Y., Yoshida, N., & Ceverino, D. 2023, ApJ, 953, 140, doi: [10.3847/1538-4357/ace25a](https://doi.org/10.3847/1538-4357/ace25a)

Nanni, A., Romano, M., Donevski, D., et al. 2025, arXiv e-prints, arXiv:2505.10701, doi: [10.48550/arXiv.2505.10701](https://doi.org/10.48550/arXiv.2505.10701)

Narayanan, D., Davé, R., Johnson, B. D., et al. 2018a, MNRAS, 474, 1718, doi: [10.1093/mnras/stx2860](https://doi.org/10.1093/mnras/stx2860)

—. 2018b, MNRAS, 474, 1718, doi: [10.1093/mnras/stx2860](https://doi.org/10.1093/mnras/stx2860)

Narayanan, D., Stark, D. P., Finkelstein, S. L., et al. 2025a, ApJ, 982, 7, doi: [10.3847/1538-4357/adb41c](https://doi.org/10.3847/1538-4357/adb41c)

Narayanan, D., Torrey, P., Stark, D., et al. 2025b, arXiv e-prints, arXiv:2509.18266, doi: [10.48550/arXiv.2509.18266](https://doi.org/10.48550/arXiv.2509.18266)

Newman, S. L., Lovell, C. C., Maraston, C., et al. 2026, MNRAS, 545, staf1866, doi: [10.1093/mnras/staf1866](https://doi.org/10.1093/mnras/staf1866)

Ormerod, K., Witstok, J., Smit, R., et al. 2025, arXiv e-prints, arXiv:2502.21119, doi: [10.48550/arXiv.2502.21119](https://doi.org/10.48550/arXiv.2502.21119)

Ostriker, E. C., & Shetty, R. 2011, ApJ, 731, 41, doi: [10.1088/0004-637X/731/1/41](https://doi.org/10.1088/0004-637X/731/1/41)

Pallottini, A., Ferrara, A., Gallerani, S., et al. 2022, MNRAS, 513, 5621, doi: [10.1093/mnras/stac1281](https://doi.org/10.1093/mnras/stac1281)

Parlanti, E., Carniani, S., Venturi, G., et al. 2025, A&A, 695, A6, doi: [10.1051/0004-6361/202451692](https://doi.org/10.1051/0004-6361/202451692)

Pforr, J., Maraston, C., & Tonini, C. 2012, MNRAS, 422, 3285, doi: [10.1111/j.1365-2966.2012.20848.x](https://doi.org/10.1111/j.1365-2966.2012.20848.x)

Planck Collaboration, Ade, P. A. R., Aghanim, N., et al. 2014, A&A, 571, A16, doi: [10.1051/0004-6361/201321591](https://doi.org/10.1051/0004-6361/201321591)

Popping, G., Puglisi, A., & Norman, C. A. 2017, MNRAS, 472, 2315, doi: [10.1093/mnras/stx2202](https://doi.org/10.1093/mnras/stx2202)

Punyasheel, P., Vijayan, A. P., Greve, T. R., et al. 2025, A&A, 696, A234, doi: [10.1051/0004-6361/202452040](https://doi.org/10.1051/0004-6361/202452040)

Rosolowsky, E. W., Pineda, J. E., Kauffmann, J., & Goodman, A. A. 2008, ApJ, 679, 1338, doi: [10.1086/587685](https://doi.org/10.1086/587685)

Rowland, L. E., Hodge, J., Bouwens, R., et al. 2024, MNRAS, 535, 2068, doi: [10.1093/mnras/stae2217](https://doi.org/10.1093/mnras/stae2217)

Saxena, A., Cameron, A. J., Katz, H., et al. 2024, arXiv e-prints, arXiv:2411.14532, doi: [10.48550/arXiv.2411.14532](https://doi.org/10.48550/arXiv.2411.14532)

Schreiber, C., Elbaz, D., Pannella, M., et al. 2018, A&A, 609, A30, doi: [10.1051/0004-6361/201731506](https://doi.org/10.1051/0004-6361/201731506)

Seon, K.-I., & Draine, B. T. 2016, ApJ, 833, 201, doi: [10.3847/1538-4357/833/2/201](https://doi.org/10.3847/1538-4357/833/2/201)

Shibuya, T., Ito, Y., Asai, K., et al. 2024, arXiv e-prints, arXiv:2403.06729, doi: [10.48550/arXiv.2403.06729](https://doi.org/10.48550/arXiv.2403.06729)

Shivaei, I., Naidu, R. P., Rodríguez Montero, F., et al. 2025, arXiv e-prints, arXiv:2509.01795, doi: [10.48550/arXiv.2509.01795](https://doi.org/10.48550/arXiv.2509.01795)

Sommovigo, L., Ferrara, A., Carniani, S., et al. 2021, MNRAS, 503, 4878, doi: [10.1093/mnras/stab720](https://doi.org/10.1093/mnras/stab720)

Sommovigo, L., Ferrara, A., Pallottini, A., et al. 2022, MNRAS, 513, 3122, doi: [10.1093/mnras/stac302](https://doi.org/10.1093/mnras/stac302)

Stanway, E. R., & Eldridge, J. J. 2018, MNRAS, 479, 75, doi: [10.1093/mnras/sty1353](https://doi.org/10.1093/mnras/sty1353)

Sugahara, Y., Álvarez-Márquez, J., Hashimoto, T., et al. 2025, ApJ, 981, 135, doi: [10.3847/1538-4357/adb02a](https://doi.org/10.3847/1538-4357/adb02a)

Sun, F., Helton, J. M., Egami, E., et al. 2024, ApJ, 961, 69, doi: [10.3847/1538-4357/ad07e3](https://doi.org/10.3847/1538-4357/ad07e3)

Tanaka, T. S., Silverman, J. D., Nakazato, Y., et al. 2024, PASJ, 76, 1323, doi: [10.1093/pasj/pse091](https://doi.org/10.1093/pasj/pse091)

Topping, M. W., Stark, D. P., Endsley, R., et al. 2022, ApJ, 941, 153, doi: [10.3847/1538-4357/aca522](https://doi.org/10.3847/1538-4357/aca522)

—. 2024, MNRAS, 529, 4087, doi: [10.1093/mnras/stae800](https://doi.org/10.1093/mnras/stae800)

Toyouchi, D., Yajima, H., Ferrara, A., & Nagamine, K. 2025, arXiv e-prints, arXiv:2502.12538, doi: [10.48550/arXiv.2502.12538](https://doi.org/10.48550/arXiv.2502.12538)

Tsukui, T., Wisnioski, E., Krumholz, M. R., & Battisti, A. 2023, MNRAS, 523, 4654, doi: [10.1093/mnras/stad1464](https://doi.org/10.1093/mnras/stad1464)

Tsuna, D., Nakazato, Y., & Hartwig, T. 2023, MNRAS, 526, 4801, doi: [10.1093/mnras/stad3043](https://doi.org/10.1093/mnras/stad3043)

Vijayan, A. P., Clay, S. J., Thomas, P. A., et al. 2019, MNRAS, 489, 4072, doi: [10.1093/mnras/stz1948](https://doi.org/10.1093/mnras/stz1948)

Villanueva, V., Herrera-Camus, R., González-López, J., et al. 2024, A&A, 691, A133, doi: [10.1051/0004-6361/202451490](https://doi.org/10.1051/0004-6361/202451490)

Weingartner, J. C., & Draine, B. T. 2001, ApJ, 548, 296, doi: [10.1086/318651](https://doi.org/10.1086/318651)

Witstok, J., Smit, R., Maiolino, R., et al. 2022, MNRAS, doi: [10.1093/mnras/stac1905](https://doi.org/10.1093/mnras/stac1905)

Witstok, J., Shivaei, I., Smit, R., et al. 2023, Nature, 621, 267, doi: [10.1038/s41586-023-06413-w](https://doi.org/10.1038/s41586-023-06413-w)

Xu, C., & Buat, V. 1995, A&A, 293, L65, doi: [10.48550/arXiv.astro-ph/9411101](https://doi.org/10.48550/arXiv.astro-ph/9411101)

Yanagisawa, H., Ouchi, M., Nakajima, K., et al. 2025, ApJ, 988, 86, doi: [10.3847/1538-4357/adcecd](https://doi.org/10.3847/1538-4357/adcecd)

Zhukovska, S., Gail, H. P., & Trieloff, M. 2008, A&A, 479, 453, doi: [10.1051/0004-6361:20077789](https://doi.org/10.1051/0004-6361:20077789)